Professor Ralf Vanselow
Department of Chemistry and Laboratory for Surface Studies,
The University of Wisconsin-Milwaukee,
Milwaukee, WI 53201, USA

Dr. Russell Howe
Department of Chemistry, University of Auckland,
Private Bag, Auckland, New Zealand

Series Editors

Professor Dr. Gerhard Ertl
Fritz-Haber-Institut der Max-Planck-Gesellschaft, Faradayweg 4–6
D-1000 Berlin 33

Professor Robert Gomer
The James Franck Institute, The University of Chicago, 5640 Ellis Avenue,
Chicago, IL 60637, USA

Managing Editor

Dr. Helmut K. V. Lotsch
Springer-Verlag, Tiergartenstrasse 17,
D-6900 Heidelberg, Fed. Rep. of Germany

ISBN 3-540-50044-8 Springer-Verlag Berlin Heidelberg New York
ISBN 0-387-50044-8 Springer-Verlag New York Berlin Heidelberg

Offsetprinting: Druckhaus Beltz, 6944 Hemsbach/Bergstr.
Bookbinding: J. Schäffer GmbH & Co. KG., 6718 Grünstadt
2154/3150-543210 Printed on acid free paper

R. Vanselow R. F. Howe (Eds.)

Chemistry and Physics of Solid Surfaces VII

With 315 Figures

Springer-Verlag Berlin Heidelberg New York
London Paris Tokyo

2. Physisorbed Rare Gas Adlayers

Klaus Kern and George Comsa

Institut für Grenzflächenforschung und Vakuumphysik
Kernforschungsanlage Jülich, D – 5170 Jülich, Fed. Rep. Germany

Within the Born-Oppenheimer approximation, the motion of a rare gas atom in front of a substrate surface can be described with a three dimensional potential energy relief, depending on two coordinates parallel $V(x,y)$ and one perpendicular to the surface $V(z)$. Since the electron affinity of the rare gases is negative and their ionization energy is large compared to the work function of almost all substrates, the electronic configuration of the rare gas atom is only slightly perturbed upon adsorption. Thus, rare gases interact with substrates mainly via induced dipole forces (van der Waals interaction), which can be modelled by a superposition of a long-range van der Waals attractive term (decaying as z^{-3}) and a short range repulsive term. The corresponding adsorption potential is shown in Fig.2.1; the minimum of $V(z)$ determines the adsorption energy in the limit of zero coverage. Particles which are bound to surfaces via these dispersion forces are called physisorbed. Typical physisorption energies range from several to hundreds of meV.

At low coverages, the state of the adsorbate is determined by the magnitude of the potential modulation $V(x,y)$ and the temperature. For temperatures which are large compared to the modulation energy, the adparticle can move freely on the surface. However, if the temperature is small compared to the modulation, the adparticle is fixed to its

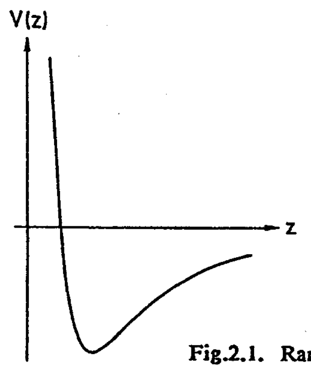

Fig.2.1. Rare-gas-surface interaction potential

adsorption site, i.e., the adsorption is localized. With increasing coverage, however, the mutual interactions between the adatoms gain importance. These interactions can be either direct or substrate mediated, repulsive or attractive in nature. It is the competition between these lateral adatom interactions and the potential modulation V(x,y) which gives rise to a variety of phase transitions in the adsorbed layer. Phase transition is defined here as a change of the pair correlation function by changing the long range order, i.e., the structure, of the adlayer.

Physisorbed rare gas layers have attracted much interest during the last decade. This is not only because their investigation gives access to fundamental processes like condensation, melting or polymorphism, in low dimensional systems (2D) exhibiting enhanced fluctuation effects, but also because, from a theoretical point of view, the simple interaction forces allow first principle calculations.

Peierls [2.1] and *Landau* [2.2] discovered as early as the 30's that solids in two dimensions exhibit a number of remarkable properties. They demonstrated that for a 2D-solid the pair correlation function diverges algebraically at any finite temperature, i.e., strictly speaking, there should be no crystalline order in two dimensions. This rather spectacular observation remained almost unnoticed for decades. Today's interest in 2D-matter started with the remarkable studies of *Wegner* [2.3], *Jancovici* [2.4] and *Kosterlitz* and *Thouless* [2.5] in the late 60's and early 70's. In particular, *Kosterlitz* and *Thouless* [2.5] proposed a new criterion for crystalline order in two dimensions, "topological long-range order". Even if true long-range positional order does not exist, the crystalline axes could still be well defined, i.e., the angle that the bond between two adjacent atoms makes with some reference axis is an order parameter, and one can have bond orientational long-range order. Provided the shear modulus, μ, is finite, a two dimensional arrangement of atoms with long-range orientational order and algebraic positional order exhibits enough short- to medium-range order for a local crystalline structure to be defined. However, we should mention that the Peierls-Landau instability is almost negligible as long as we deal with crystallites less than say $\simeq$200 nm in diameter. Indeed, as pointed out by *Abraham* [2.6], a 2D-solid has to be as large as $\simeq 10^{27}$ cm^2 in order to lose crystalline correlation equal to about one lattice spacing.

The resistance to shear is probably the best definition of a solid. *Kosterlitz* and *Thouless* [2.5] argued that at low temperatures there are no free dislocations present and hence the 2D-system is a "crystalline solid". In two dimensions, a dislocation is a defect in a perfect crystal in which half an extra row of atoms is added. At a certain temperature T_m, however, the free energy for spontaneous formation of free dislocations becomes negative, and the 2D-system will no longer resist shear, because an arbitrarily small shear stress will cause the free dislocations to move. Based on this concept, *Kosterlitz* and *Thouless* [2.5], *Halperin* and *Nelson* [2.7], and *Young* [2.8] developed a theory of two dimensional melting, initiating much of the current interest in 2D-solids. In contrast to 3D-systems, where melting is definitely a first order transition, they predicted that in two dimensional systems it has to be a second order one.

In addition, fascinating properties of 2D-solids arise from the fact that in experiment, any 2D-solid needs to be supported by a substrate. The physisorbed atoms form a modulated structure on the lattice of the substrate surface. The modulation arises from the competing interactions which favor different periodicities; the "natural" nearest-neighbor distance of the nonsupported adlayer differs in general from the lattice periodicity which the substrate potential tries to impose. The physisorbed adatoms form in general ordered structures. These may be commensurate with the substrate surface in certain ranges of coverage and temperature. However, when coverage and/or temperature is varied, the adlayer may contract or expand and become incommensurate with the supporting substrate. According to the present understanding of theory [2.9] these kind of phase transitions are driven by the spontaneous formation of misfit dislocations, so called domain walls.

The interest in adsorbed layers is not restricted to the understanding of fundamental two dimensional physics. As such films increase in thickness, they finally approach three dimensional behavior. The manner in which thin films grow is of great practical importance in various processes like adhesion, lubrication or production of submicron electronic devices. Investigation of the evolution from 2D to 3D behavior of rare gases is the most straightforward experiment to uncover the fundamental principles governing the growth properties.

After discussing the present status of the experimental techniques, we will examine structure, phase diagrams, phase transitions and lattice dynamics of physisorbed layers of the heavy rare gases Kr and Xe on a single crystal Pt{111} surface.

2.1 Experimental Techniques

2.1.1 General Remarks

The above discussion raises one main question: how can one probe the structure and dynamics of physisorbed adlayers with enough sensitivity and without disturbing these delicate systems? The most direct way to get such information is via a scattering experiment, the basic principle of which is illustrated in Fig.2.2. An incoming beam of probe particles

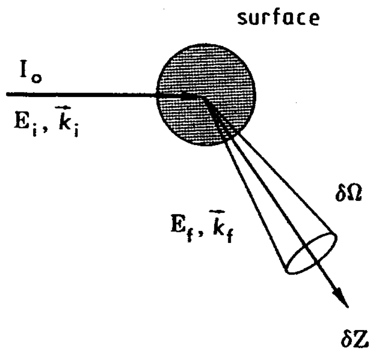

Fig.2.2. Schematic sketch of a surface scattering experiment

(e.g., electrons, photons, neutrons or atoms) of wavevector $\mathbf{k}_i$ and energy E_i, impinges on a target, and the scattered intensity at wavevector $\mathbf{k}_f$ and energy E_f is measured in the solid angle element $\delta\Omega$. The complete information which can be deduced in such a scattering experiment, i.e., the behavior of the target particles in space and time, is contained in the double differential cross section:

$$\delta Z = I_0 \frac{d^2\sigma}{d\Omega dE_f} \delta\Omega \, \delta E_f \tag{2.1}$$

where δZ is the number of probe particles in the energy interval δE_f scattered into the solid angle element $\delta\Omega$, and I_0 the intensity of the incoming probe particles. Except for trivial factors, the scattering cross section is determined by the energy exchange ($\hbar\omega$) and the momentum exchange (Q).

$$\frac{d^2\sigma}{d\Omega dE_f} \simeq S(Q,\hbar\omega)$$

$$\hbar\omega = E_f - E_i\,, \quad \mathbf{Q} = \mathbf{k}_f - \mathbf{k}_i \tag{2.2}$$

The selection of the probe particles is determined by the characteristic energy, time and length scales of the phenomena to be investigated. In Table 2.1, we have collected a few characteristic parameters for physisorbed films of rare gases. In order to gain information on these different processes in a scattering experiment it is favorable when energy and momentum of the probe particles simultaneously match the characteristic parameters of the surface processes (energy, $\hbar\omega$, time, $1/\omega$, and length, $1/Q$). For particle waves (electrons, neutrons and atoms) the de Broglie relation gives $\lambda = \hbar/(2mE)^{1/2}$ whereas for electromagnetic waves (photons) the dispersion relation is $\lambda = \hbar c/E$. In Fig.2.3 we illustrate this wavelength-energy dispersion for the different probe particles. Obviously, the wavelength-energy range accessible to electrons, neutrons and He atoms, coincides with the energy and time-scales which are characteristic for collective excitations and atomic

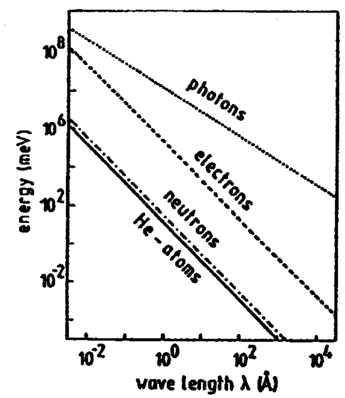

Fig.2.3. Wavelength-energy dispersion of non-relativistic particles (electrons, neutrons, He atoms) and electromagnetic waves (photons)

Table 2.1 Characteristic parameters of processes in physisorbed rare gas films.

energy-scale		
	adsorption energy	5-300 meV
	phonons	0.1-10 meV
time-scale		
	elemental step of diffusion	$> 10^{-12}$ s
	phonon lifetime	$> 10^{-11}$ s
length-scale		
	lattice parameter	3-5 Å
	correlation length	10-5000 Å
	phonon wavelength (at the zone boundary)	≥ 1 Å

movements on the surface. On the other hand, for electromagnetic waves this coincidence is absent, generally $\hbar\omega$ and Q do not match.

The most convenient way to obtain structural information is via a diffraction experiment: a beam of well-defined wavelength impinges on a target, and the elastically scattered intensity is measured by an appropriate detector. For diffraction from a periodic two dimensional arrangement of atoms the structure factor $S(Q,\hbar\omega = 0)$ denotes:

$$S(Q,0) = \sum_m \delta(Q^{\parallel} - G_m^{\parallel}). \tag{2.3}$$

The terms $Q^{\parallel} = (Q_x, Q_y)$ and $G_m^{\parallel} = (G_{mx}, G_{my})$ are the momentum exchange vector and the reciprocal lattice vector in the surface plane of the two-dimensional structure, respectively. Thus, the Laue-condition for diffraction from a 2D-lattice reads

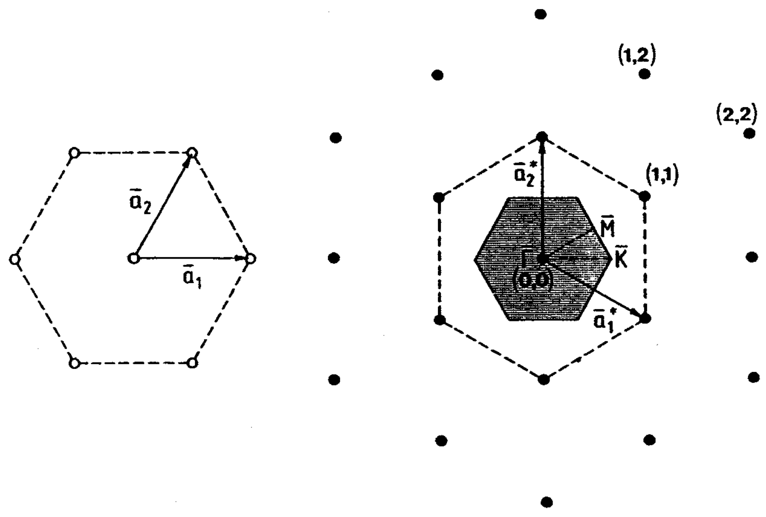

Fig.2.4. Real lattice (left) and reciprocal lattice (right) of a triangular 2D-net

$$Q^{\parallel} = G_m^{\parallel} \quad (2.4).$$

In Fig.2.4, we show as an example the real and reciprocal space for the densest possible arrangement in a periodic 2D-lattice, the triangular lattice, which is the most widespread structure of ordered rare-gas adlayers and also the structure of the (111)-face of fcc crystals. The high symmetry points in the reciprocal lattice are denoted by $\bar{\Gamma}$, $\bar{M}$, and $\bar{K}$; the hatched area is the first Brillouin zone.

2.1.2 Probe Particles

The most stringent requirement for probe particles when used in studies of adsorbed overlayers is an adequate surface sensitivity. From this point of view, thermal He atoms are the most appropriate probe particles. Because of their large cross section, thermal atoms of small energy (<100 meV) interact with the outermost layer only; there is no penetration into deeper layers. The classical turning point of thermal energy He atoms is usually about 0.3 nm above the ion cores of the outermost layer.

In the energy range used in low energy electron diffraction (LEED), 10-1000 eV, the information depth is between 0.4 and 1 nm. This surface sensitivity of low energy electrons is mainly due to the large cross section for inelastic scattering. For high energy electrons (RHEED), X-rays, or neutrons, the information depth is normally much larger. Surface sensitivity in these cases can be obtained either

by using grazing incidence- and exit-angles (high energy electrons and X-rays) or by using substrates with large surface to volume ratio like powdered samples to discriminate against background scattering (neutrons and X-rays). In the case of neutrons or X-rays, particular adsorbate/substrate combinations are chosen in which the scattering cross-sections of the adsorbate nuclei are much larger than those of the substrate.

a) Electrons

Electrons are the most widely used surface analytical probe particles [2.10]. Clean as well as adsorbate covered surfaces are routinely investigated by techniques like LEED, Auger electron spectroscopy (AES) or electron energy loss spectroscopy (EELS). The main concern when an electron beam is incident on a rare gas adlayer is the large cross section for electron stimulated desorption; its effect has to be carefully checked. Whereas LEED and AES are currently applied to the study of physisorbed phases at low temperatures, EELS has not been used so far. The reason is of a technical rather than fundamental nature. Although the momentum-energy range (Fig.2.3) covered by low energy electrons is suited for studies of collective lattice excitations, the energy resolution ($\simeq$4 meV for these electrons) [2.11] is not sufficient to resolve these excitations in physisorbed films. This energy resolution is, however, good enough to study the internal vibrational modes of physisorbed molecules. Some experimental arrangements are currently set up to investigate this interesting subject.

In a typical experimental arrangement for the study of physisorbed films by electron diffraction [2.12,13], the LEED-optics (channelplate detector) is optimized for low electron beam currents in the nanoampere range in order to avoid electron stimulated desorption or local heating of the weakly bound films. The momentum resolution of a typical LEED-system is about 0.1 nm^{-1} (FWHM). However, very recently, instruments capable of very high resolution have been developed [2.14,15]. Another very promising improvement of LEED, invented recently by *Telieps* and *Bauer*, is the low energy electron microscopy (LEEM) [2.16]. In this technique, the surface is imaged with diffracted low-energy electrons. The lateral resolution obtainable is about 10 nm. Although this technique has been used so far only for the study of phase transitions on clean surfaces and metal layers, it should also be applicable to physisorbed films.

In recent years, the RHEED technique has been very popular in characterizing the type of multilayer growth [2.17]. However, the soundness of the interpretation of RHEED-patterns (streaks $\rightarrow$ perfectly flat surface; sharp spots $\rightarrow$ 3D-crystallites on the surface) has been severely challenged of late [2.18].

b) Neutrons

Among the probes currently used in condensed matter studies, neutrons have a unique status. Since the wavelength and energy of thermal neutrons are comparable with interatomic distances in condensed phases and with characteristic energies of most crystal atom motions, neutrons are the most versatile probe of bulk matter. Their application to surface studies, however, requires the use of high surface area materials, like Grafoil or powdered MgO, because of the weak scattering of neutrons by matter. These kind of substrates certainly have some disadvantages; they tend to have surface inhomogeneities and orientational ordering effects cannot be studied. On the other hand, there are also some advantages of the weak scattering: experiments can be done at high ambient pressures and on technologically important samples like raney-nickel or zeolites.

Typical momentum resolution obtained with neutron spectrometers are 0.05-0.1 nm^{-1} whereas the energy resolution can be as good as 1 μeV [2.19]. This extreme energy resolution allows, for instance, the measurement of rotational tunneling energies of adsorbed molecules, not accessible so far to any other method. Numerous physisorption systems have been investigated with neutron scattering. A large amount of information on the atomic arrangement in the adsorbed layer, distance of the layer from the substrate, intramolecular structure of the adsorbed species, collective excitations within the adsorbed layer, rotational and vibrational spectroscopy of adsorbed molecules, etc., has been obtained. An extended review on this subject has been given by *Thomas* [2.19]. A particularly interesting application of the technique, the incoherent quasielastic scattering, has been used recently by *Bienfait* [2.20] to study the diffusive motion of CH_4 films adsorbed on MgO to gain insight into the surface melting of these films.

c) X-Ray Photons

The recent rapid development of surface structural tools based on X-ray photons as probe particles is linked to the development of bright X-ray sources with the advent of synchrotron radiation. However, as already noted, X-rays only interact weakly with condensed-matter, and thus it is necessary to develop techniques which allow a separation between surface and bulk scattering. In the case of clean surfaces, this can only be done by using grazing angles of incidence; a technique which has been developed recently by *Eisenberger* and *Marra* [2.21]. In the case of adsorbed layer studies, however, glancing angles may be avoided by choosing a strongly scattering adsorbate on a weakly scattering substrate. Because the scattering cross-section scales with the square of the atomic number, the heavier noble gases adsorbed on the basal plane of graphite, for instance, are an appropriate choice. With a

typical X-ray scattering spectrometer for physisorbed film studies (beam energy $\simeq$ 10 keV), which has been installed at Stanford Synchrotron Radiation Laboratory [2.22], the adsorbed layer to substrate scattering ratio for a commensurate Kr monolayer on the basal plane of graphite was $\simeq$600/150.

The important advantage of the use of synchrotron X-ray diffraction lies in the fact that the scattering can be interpreted in the kinematic approximation and that momentum resolution of the order 0.001 nm^{-1} can be obtained routinely. This very high resolution allows the study of spatial correlations from 1 nm to 1000 nm via line shape analysis of the diffraction peaks [2.23]. Also, like neutrons, X-rays are not restricted to low ambient pressures as electrons or He atoms are.

The main limitation in the use of X-rays in the study of thin physisorbed films stems from the discrepancy between the energy of the X-ray photons and the energy of collective phenomena in the adlayers. Although *Burkel* and coworkers [2.24] have recently measured optical phonons in pyrolytic graphite and in Be single crystals by means of inelastic scattering of X-rays, this technique will not be applicable to physisorbed films in the near future. The present limit for the absolute energy resolution is about 8 meV, which is twice as large as that of EELS.

d) Helium Atoms

The recent progress in generation of highly monochromatic He nozzle beams [2.25,26] and their combination with ultrahigh vacuum techniques has favored the development of several novel surface analytical tools based on the interaction of thermal He atoms with solid surfaces. He atom scattering is one of the oldest surface probes [2.27]. However, the lack of an appropriate He-beam source was the main hurdle in the development of this now very powerful analytical tool. For a long time the Knudsen (effusion) cell was the only means for producing molecular beams. The Maxwellian effusive beams have low intensity ($I_0 \simeq 10^{14}$ particles $s^{-1}sr^{-1}$ and low monochromaticity ($\Delta v/v = \Delta\lambda/\lambda = 0.95$). Monochromaticity improvement by means of mechanical velocity selectors reduces the already low intensity to a level almost unacceptable for the requirements of surface analysis. The major break-through was the development of high pressure nozzle sources. The effect achieved by the invention of these sources is only comparable to that of the laser technology: simultaneous increase of intensity and monochromaticity by several orders of magnitude. Indeed, intensities of 10^{19} particles $s^{-1}sr^{-1}$ and monochromaticities of $\Delta v/v = \Delta\lambda/\lambda \simeq 0.007$ are obtained routinely today (Fig.2.5). The beam monochromaticity is the result of the large number of collisions in the hydrodynamic expansion of a gas: the larger the number of collisions, the higher the monochromaticity;

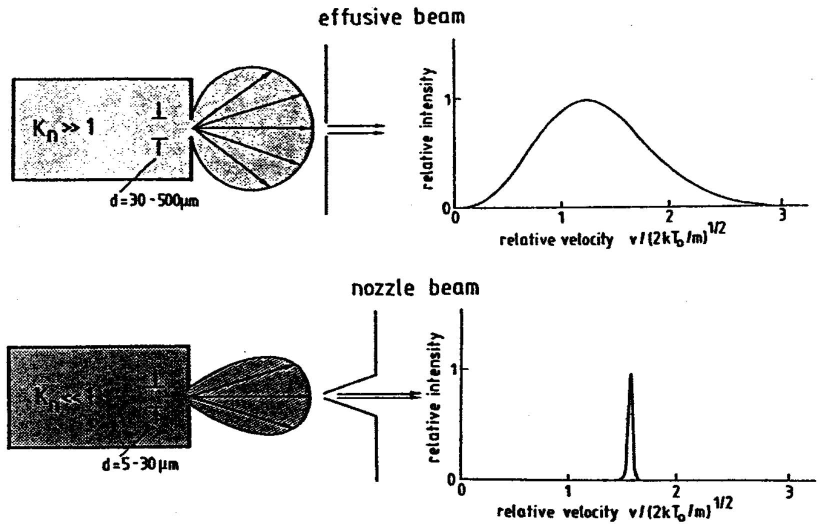

Fig.2.5. Comparison of effusive and nozzle-beam systems

i.e., the smaller the half width of the velocity distribution. Accordingly, high monochromaticity is obtained by using large stagnation gas pressures and/or low stagnation temperature. The latter increases the number of collisions because, at low relative velocities, the collision cross-section of atoms increases. Due to quantum effects, this increase is particularly pronounced for helium [2.28].

For a 20 meV He-beam, a velocity spread of $\Delta v/v \simeq 0.007$ corresponds to an energy spread smaller than 0.3 meV (FWHM), a value close to the energy resolution in optical spectroscopies. Note that even in the case of He the beam monochromaticity cannot be increased by cooling beyond a certain limit. For stagnation temperatures less than $\simeq$30 K, the onset of clustering may destroy the beam properties [2.29].

The major characteristics of the He-beam as surface analytical tool are connected with the nature of the He-surface interaction potential. At distances not too far from the surface, the He atom is weakly attracted due to dispersion forces. At a closer approach, the electronic densities of the He atom and of the surface atoms overlap, giving rise to a strong repulsion. The classical turning point for thermal He is a few Angstroms in front of the outermost surface layer. It is this interaction mechanism which makes the He-beam an outstanding surface tool, sensitive exclusively to the outermost layer. The low energy of the He atoms and their inert nature ensures that He scattering is a completely nondestructive surface probe. This is particularly important when delicate phases, like rare-gas layers, are investigated.

The de Broglie wavelength of thermal He atoms is comparable with the interatomic distances in adsorbed overlayers. Thus, from measurements of the angular positions of the diffraction-peaks the size and orientation of the 2D unit cell, i.e., the structure of the outermost layer can be straightforwardly determined. Analysis of the peak intensities yield the potential corrugation, which usually reflects in a direct way the geometrical arrangement of the atoms within the 2D unit cell [2.30].

The energy of thermal He atoms is comparable to the energies of collective excitations in overlayers. Thus, in a scattering experiment, the He atom may exchange an appreciable part of its energy with the surface. This energy can be measured in time-of-flight experiments with a resolution $\simeq$0.3 meV, more than 10 times better than with EELS [2.31]. Thus, surface phonon dispersion curves of rare-gas layers can be mapped out by measuring energy loss spectra at various momentum transfers in different crystallographic directions. This is a definite advantage of inelastic He-scattering over inelastic neutron scattering. (In view of the random orientation of powdered samples, which have to be used in neutron scattering, only average phonon density of states, but not dispersion curves can be obtained.) The range of energy transfer that can be covered by thermal He-atoms is limited at the low end by the present maximum resolution of $\simeq$0.3 meV and at the high end by the nature of the scattering mechanism. The He-beam surface interaction time being finite, the upper limit for the detectable phonon energy is about 40 meV. So far, only modes with a component perpendicular to the surface have been clearly detected; this seems to be less a fundamental than a technical problem.

Besides the inelastic component, a certain fraction of the elastically scattered He atoms are always found between the coherent diffraction peaks. We will refer to this scattering as diffuse elastic scattering. This diffuse intensity is attributed to scattering from defects and impurities. Accordingly, this diffuse elastic scattering provides valuable information on the degree and nature of surface disorder. It can be used, for example, to study the growth of thin films [2.32] or to deduce information on the size, nature and orientation of surface defects [2.33]. Very recently, the peak shape analysis of the diffuse elastic component has also been used to study the diffusive motion of surface atoms [2.34].

Another remarkable way to use He-scattering for the study of adsorbed layers is based on the large total cross section for diffuse He-scattering of isolated adsorbates (e.g., $\Sigma_{Xe}^{He} \simeq 1.1$ nm^2 for E_{He}=18 meV). This large cross section is attributed to the long-range attractive interaction which causes He atoms to be scattered out of the (0,0) beam. This extreme sensitivity of He-beams allows the extraction of important information concerning the lateral distribution of adsorbates, mutual interactions between adsorbates, dilute-condensed phase transitions in 2D, adatom mobilities, etc. [2.35], simply by monitoring the attenuation of the (0,0) He-beam, i.e., the specular beam. This technique also allows the detection of impurities (including hydrogen!) in the per mille range, a level hardly attainable with almost all other methods.

The type of information that can be derived by He atom scattering from physisorbed adlayers is summarized in Table 2.2, together with the type of scattering involved.

In Fig.2.6 we show a schematic sketch of the high resolution He-scattering spectrometer used in the authors' laboratory for studies of thin physisorbed films [2.36]. The scattering geometry is fixed with $\theta_i+\theta_f = 90^0$, where θ_i and θ_f are the incident and outgoing angles, respectively. The vacuum system consists of four main units: the three-chamber nozzle-beam generator, the scattering chamber (with sample holder, LEED, CMA-Auger, and ion gun facilities), the pseudorandom chopper chamber, and the three-chamber detector unit. The scattering chamber has a base pressure in the low 10^{-11} mbar range which rises to about 10^{-9} mbar (He partial pressure) during He-beam operation. The extensive differential pumping serves to reduce the He-partial base pressure in the detector chamber to 10^{-15}-10^{-16} mbar. As a detector we use a commercial Extranuclear mass spectrometer with electron bombardment ionizer; the residual He-pressure in the detector chamber results in a count rate of about 40 counts/s at 5mA emission

Table 2.2 Types of He atom scattering from overlayers and information which can be inferred

Type of scattering	Energy and parallel momentum exchange	Information
diffraction	$\hbar\omega = 0$ $Q^{\parallel} > 0$ (= G_m)	layer structure, orientational ordering, correlation lengths, distance of layer from substrate, random step densities
specular	$\hbar\omega = 0$ $Q^{\parallel} = 0$ (= G_0)	thermodynamics, impurity and defect densities, lateral distribution of adsorbates, adatom mobility
inelastic	$\hbar\omega \neq 0$ $Q^{\parallel} > 0$	collective excitations within adsorbed layer, dynamical coupling between layer and substrate
diffuse elastic	$\hbar\omega = 0$ $Q^{\parallel} > 0$ ($\neq G_m$)	layer perfectness; growth mode; size, nature and orientation of surface defects; surface diffusion

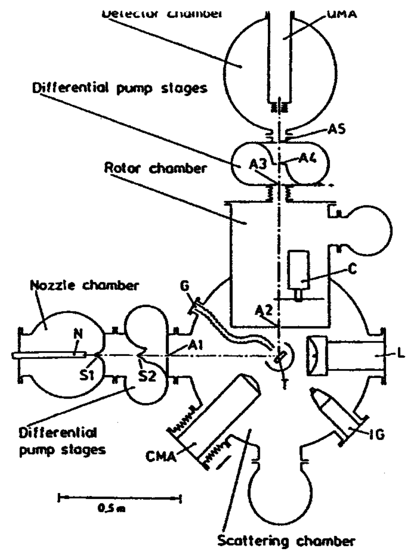

Fig.2.6. Schematic diagram of a high resolution He time-of-flight spectrometer. (N: nozzle beam source, S1,2: skimmers, A1-5: apertures, T: target, G: gas doser, CMA: Auger spectrometer, IG: ion gun, L: LEED, C: Magnetically suspended pseudorandom chopper, QMA: detector, quadrupole mass analyzer with channeltron)

current. This figure has to be compared with 10^5 counts/s, representing the signal of the first order He-diffraction beam (E_{He}=18 meV) from a Kr monolayer adsorbed on Pt {111} at 25 K.

In most experiments a 18 meV He-beam, produced by cooling the nozzle with liquid nitrogen, is used. The particle flux impinging on the target is about $2 \cdot 10^{19}$ He atoms $s^{-1}sr^{-1}$ with a velocity spread $\Delta v/v$ = 0.007 (He stagnation pressure: 150 bar). The beam divergence as well as the acceptance angle of the detector are 0.2°. Accordingly, the overall momentum resolution of the apparatus is about 0.1 nm^{-1}, corresponding to a transfer width for the higher order peaks around 20-30 nm. Information on correlation lengths up to 100 nm can be inferred by instrumental response function deconvolution of diffraction peaks monitored with appropriate statistics.

The energy distribution of the scattered He atoms is obtained by a cross-correlation analysis of the time-of-flight (TOF) spectra of the He atoms upon passing a pseudorandom chopper [2.36,37]. At a flight path of 790 mm the overall resolution of the spectrometer for a 18 meV beam with $\Delta v/v$ = 0.007 is 0.4 meV.

The experiments reported here illustrate the 2D phase transitions and the multilayer growth of rare-gas films and are performed on a Pt{111} crystal surface as substrate. The crystal is mounted on a manipulator which allows independent polar and azimuthal rotation, as well as tilting. The temperature can be regulated between 25 and 1800 K by means of liquid He cooling and/or electron bombardment heating.

The temperature of the crystal is controlled by chromel-alumel thermocouple calibrated in situ by Xe vapor pressure isotherms monitored with surface phonon spectroscopy [2.36,38]. The Pt crystal is cleaned by repeated cycles of argon and xenon ion bombardment and annealing to 1200 K. The defect density of the clean Pt-surface is less then 10^{-3} (average terrace width 200-300 nm) as probed with elastic He scattering.

2.2 Solid-Solid Transitions in Two Dimensions

2.2.1 Commensurability

Atoms adsorbed on a periodic substrate can form ordered structures. These structures can be either in or out of registry with the structure of the substrate. It is convenient to describe this ordering by relating the Bravais lattice of the adlayer to that of the substrate surface. *Park* and *Madden* [2.39] have proposed a simple vectorial criterion to classify the structures. Let $\mathbf{a}_1$ and $\mathbf{a}_2$ be the basis vectors of the adsorbate and $\mathbf{b}_1$ and $\mathbf{b}_2$ those of the substrate surface; these can be related by

$$\begin{pmatrix} \mathbf{a}_1 \\ \mathbf{a}_2 \end{pmatrix} = G \begin{pmatrix} \mathbf{b}_1 \\ \mathbf{b}_2 \end{pmatrix} \tag{2.5}$$

with the matrix

$$G = \begin{pmatrix} G_{11} & G_{12} \\ G_{21} & G_{22} \end{pmatrix} . \tag{2.6}$$

$|\mathbf{a}_1 \times \mathbf{a}_2|$ and $|\mathbf{b}_1 \times \mathbf{b}_2|$ are the unit cell area of the adlayer and substrate surface, respectively; det G is the ratio of the two areas. The relation between the two ordered structures is classified by means of this quantity as follows:

i) *det G = integer*
the structure of the adlayer belongs to the same symmetry class as that of the substrate and is in registry with the latter; the adlayer is termed *commensurate*.

ii) *det G = irrational number*
the adlayer is out of registry with the substrate; the adlayer is termed *incommensurate*.

iii) *det G = rational number*
the adlayer is again in registry with the substrate. However, whereas in i) all adlayer atoms are located in equivalent high symmetry adsorption sites, here only a fraction of adatoms is located in equivalent sites; the adlayer is termed *high-order commensurate*.

In Fig.2.7, we show a simple one-dimensional model illustrating this classification. The periodicity of the substrate surface is provided by a sinusoidal potential of period **b** and the adlayer by a chain of atoms with nearest neighbor distance **a**.

Assuming that the structural mismatch between adlayer and substrate is not too large (≤15%), the "commensurability" is determined by the relative interaction strength h/u_c, which is the ratio of h, the lateral adatom interaction in the layer, to u_c, the modulation of the adsorbate-substrate potential parallel to the surface. It is not the whole adsorbate-substrate interaction energy, as often stated in the literature, which enters the determining ratio, but the diffusional barrier u_c. When this diffusional barrier is large compared to the lateral attraction, commensurate structures will be formed. On the other hand, when the lateral adatom interactions dominate, incommensurate structures will be favored. Only when the competing interactions are of comparable magnitude, may both registry and out of registry structures be stabilized by the complex interplay of these interactions thus leading to the occurrence of phase transitions between the various structures (Table 2.3).

We have recently measured the energetics of the adsorption of the heavy rare-gases Ar, Kr and Xe on the Pt(111) surface by means of He-scattering. In Table 2.4 we summarize the quantities pertinent to

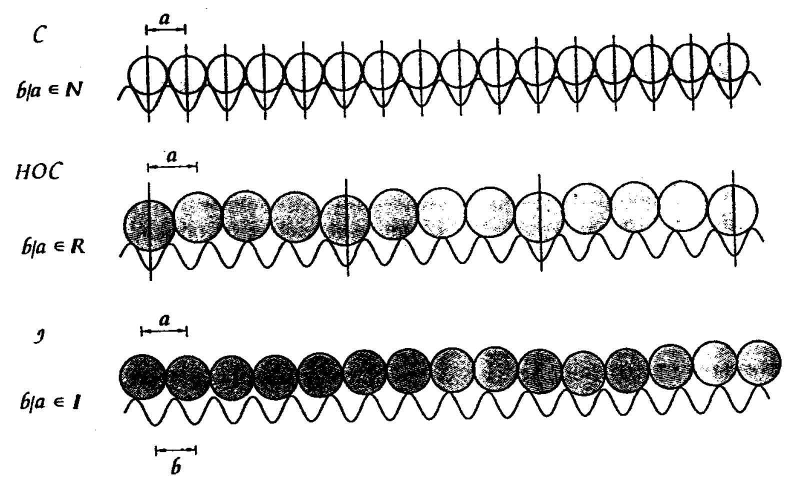

Fig.2.7. Simple one dimensional model of adsorbed adlayers. The substrate is represented by a sinosoidal potential of period b and the adlayer by a chain of atoms with nearest neighbor distance a. (C: commensurate, HOC: high order commensurate, I: incommensurate)

Table 2.3. Interaction strength h/u_c and commensurability

$h \ll u_c$	commensurate structure only
$h \gg u_c$	incommensurate structures only
$h \simeq u_c$	commensurate and incommensurate structures, corresponding phase transitions

Table 2.4. Characteristic energies of rare-gas adsorption on Pt{111} in the monolayer range

	Xe	Kr
isosteric heat q_{st} [meV] at $\theta \simeq 0$	277	128
lateral attraction h_ℓ [meV]	43	26
diffusional barrier u_c [meV]	~30	~10-20

Kr and Xe/Pt{111}. From inspection of the relevant quantities in Table 2.4 we can deduce that rare-gas monolayers on Pt{111} appear to be suited to study structural 2D-solid-solid transitions.

2.2.2 Fundamentals of the Theory Describing the Commensurate-Incommensurate Transition in 2D

The basic ideas of all modern theories of the Commensurate-Incommensurate transition are contained in the 1D model of *Frank* and *van der Merwe* (FvdM) developed in 1949 [2.40]. A linear chain of atoms with nearest neighbor distance **a** is placed in a sinusoidal potential of amplitude V and periodicity **b** representing the substrate. The mutual interaction of the atoms in the chain is assumed to be harmonic and characterized by a spring constant K. The calculations of FvdM show that for slightly different lattice parameters of chain and substrate, i.e., for a weakly incommensurate adlayer, the lowest energy state is obtained for a system which consists of large commensurate regions separated by regions of poor fit (Fig.2.8). The regions of poor lattice fit are called misfit dislocations, solitons or domain walls.

To be more quantitative we write the Hamiltonian for the linear chain problem:

$$H = \sum_n \frac{K}{2}\left(x_{n+1}-x_n-a\right)^2 + \sum_n V\cdot\left[1 - \cos\left(\frac{2\pi}{b}x_n\right)\right] \qquad (2.7)$$

where x_n is the position of the nth atom. By introducing the phase ϕ_n, which describes the positional deviation of an atom from its commensurate position

$$x_n = nb + \frac{b}{2\pi}\phi_n$$

and by approximating the discrete values ϕ_n by a continuous function $\phi(n)$, the Hamiltonian becomes

$$H = \int\left[\frac{Kb^2}{8\pi^2}\left(\frac{d\phi}{dn} - 2\pi\delta\right) + V[1 - \cos(p\phi)]\right] dn \qquad (2.9)$$

with $\delta = (a-b)/b$ being the natural misfit between adlayer and substrate and p the commensurability. The phase function ϕ for which the Hamiltonian is minimized satisfies the sine-Gordon equation:

$$\frac{d^2\phi}{dn^2} = p\,A\,\sin(p\phi) \qquad (2.10)$$

with $A = 2\pi\,(V/K)^{1/2}/b$ a solution of which is the solitary wavepacket distortion, or the so-called soliton:

$$\phi(n) = \frac{4}{p}\arctan[\exp(pn\cdot A^{1/2})]\,. \qquad (2.11)$$

The soliton solution is shown in Fig.2.8; it describes a domain wall located at n = 0 separating two adjacent commensurate regions. The soliton superlattice is a compromise between the elastic energy in the chain which favors the unperturbed incommensurate phase, and the

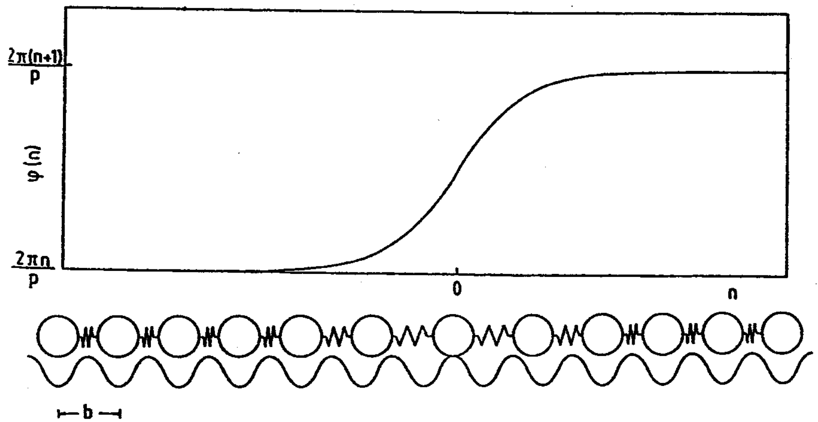

Fig.2.8. Soliton solution (domain wall) of the sine-Gordon equation. The domain wall separates two adjacent commensurate regions with $\phi = 2\pi(n+1)/p$ and $\phi = 2\pi n/p$

interaction energy with the substrate. The width of the domain wall in this model is $L_0 = 1/(pA^{1/2})$.

In two dimensional systems, walls are lines. In a triangular lattice with its C_{3v} symmetry, there are three equivalent directions. Therefore, domain walls can cross. Using Landau theory, *Bak, Mukamel, Villain,* and *Wentowska* (BMVW) [2.41] have shown that it is the wall crossing energy, Λ, which determines the symmetry of the weakly incommensurate phase and the nature of the phase transition.

i) $\Lambda < 0$, i.e., attractive walls. A hexagonal network of domain walls (HI) will be formed at the C-I transition because the number of wall crossings has to be as large as possible (Fig.2.9a). This C-HI transition should be first order.

ii) $\Lambda > 0$, i.e., repulsive walls. The number of wall crossings has to be as small as possible, i.e., a striped network of parallel walls (SI) will be formed in the incommensurate region (Fig.2.9b and c). The C-SI transition should be continuous. The striped phase is expected to be stable only close to the C-I transition. At larger misfits the hexagonal symmetry should be recovered in a first order SI$\longleftrightarrow$HI transition.

The FvdM model as well as the BMVW model neglect thermal fluctuation effects; both are T = 0 K theories. *Pokrovsky* and *Talapov* (PT) [2.42] have studied the C-SI transition including thermal effects. For $T \neq 0$ K the domain walls can meander and collide, giving rise to an entropy-mediated repulsive force between meandering walls of the form $F \propto T^2/\ell^2$, where ℓ is the distance between nearest neighbor walls. Because of this inverse square behavior, the inverse wall separation, i.e., the misfit m, in the *weakly incommensurate phase* should follow a power law of the form:

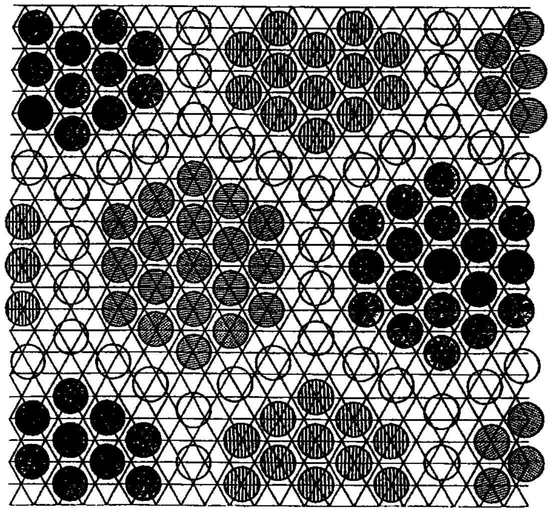

Fig.2.9a

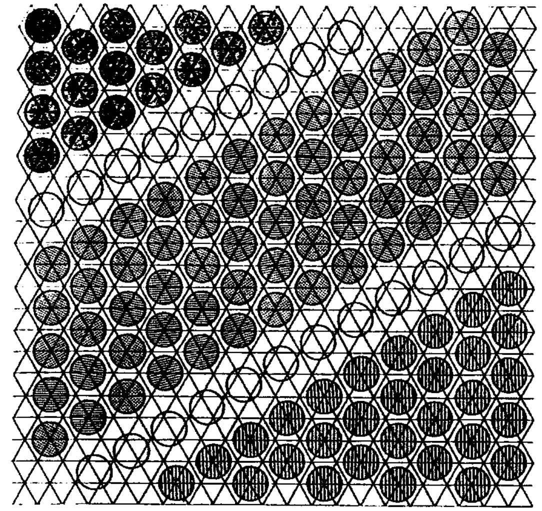

Fig.2.9b

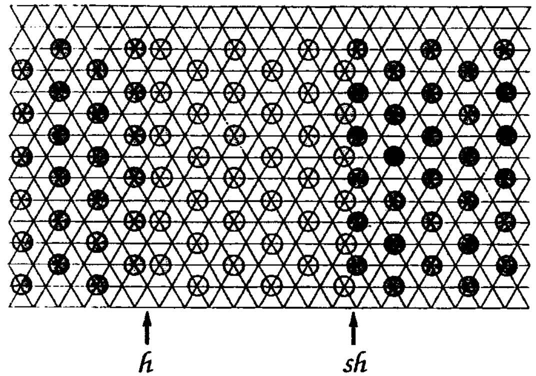

Fig.2.9c

Fig.2.9. Schematic diagram showing a) hexagonal and b) striped domain wall arrangements (in both pictures super light walls are shown). In incommensurate layers where the monolayer is compressed with respect to the commensurate lattice, domain walls are either heavy or super heavy c)

$$m = \frac{1}{\ell} \simeq \sqrt{1 - \frac{T}{T_c}} \,. \qquad (2.12)$$

2.2.3 The C-I Transition of Monolayer Xe on Pt{111}

In a recent He diffraction study [2.43] we have shown that the adsorption system Xe/Pt{111} is dominated by the existence of a $(\sqrt{3} \times \sqrt{3})$ R30° commensurate phase (Fig.2.10). The C-phase has been found to be stable in an extended temperature (62-99 K) and coverage range ($\leq 1/3$).

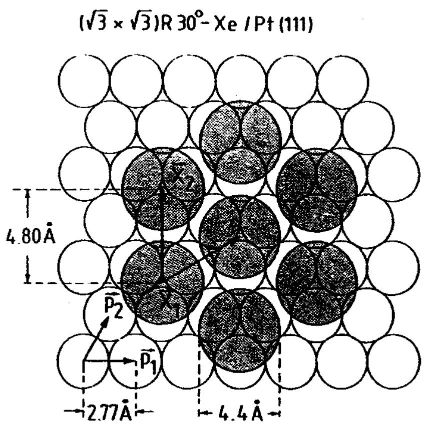

Fig.2.10. Commensurate $(\sqrt{3}x\sqrt{3})R30^o$ Xe monolayer adsorbed on Pt(111)

The maximum coverage in this $(\sqrt{3} \times \sqrt{3})$ R30° commensurate structure is obviously θ_{Xe} = 1/3 (θ_{Xe}=1 corresponds to $1.5 \cdot 10^{15}$ atoms/cm^2, the density of Pt atoms in the {111} plane). Only one third of the adsorption sites are occupied, i.e., there exist three energetically degenerate commensurate sublattices. The commensurate Xe-lattice being expanded by about 9% with respect to the "natural" Xe-lattice, the coverage can be increased beyond θ_{Xe} = 1/3. Obviously, above this limit the adatoms cannot all occupy preferred adsorption sites, and the adlayer becomes incommensurate. Alternatively, due to anharmonic effects [2.43,44], the Xe-adlayer becomes incommensurate upon decreasing the temperature below ≃ 62 K at constant coverage ($\theta_{Xe} \leq 1/3$).

Before discussing the experimental results of the C-I transition of Xe on Pt{111} in detail, let us have a look at the diffraction pattern expected from a striped (SI) and from a hexagonal uniformly (HI) compressed phase. The structures with corresponding schematic diffraction patterns are shown in Fig.2.11. The diffraction patterns for the (n,n) and (n,2n) diffraction orders are shown for fully relaxed phases.

We discuss first the basic crystallography of the incommensurate phase as deduced from the measured patterns [2.45]. Fig.2.12 shows the $(2,2)_{Xe}$ and $(1,2)_{Xe}$ diffraction features obtained from a Xe layer of coverage $\theta_{Xe} \simeq 0.30$ during the C-I transition at 54 K. The plots have been obtained by monitoring series of azimuthal scans (i.e., constant Q scans in the reciprocal space). The comparison with Fig.2.11 shows that the incommensurate Xe layer on Pt{111} is a striped phase (SI) with a uniaxial compression in the $\overline{\Gamma M}$ direction. Indeed, a three-peak structure for the $(2,2)_{Xe}$ diffraction feature, with the doublet located at $Q^{2,2}_{comm}$ + 0.048 Å^{-1} and the singlet peak located at $Q^{2,2}_{comm}$ + 0.190 Å^{-1}

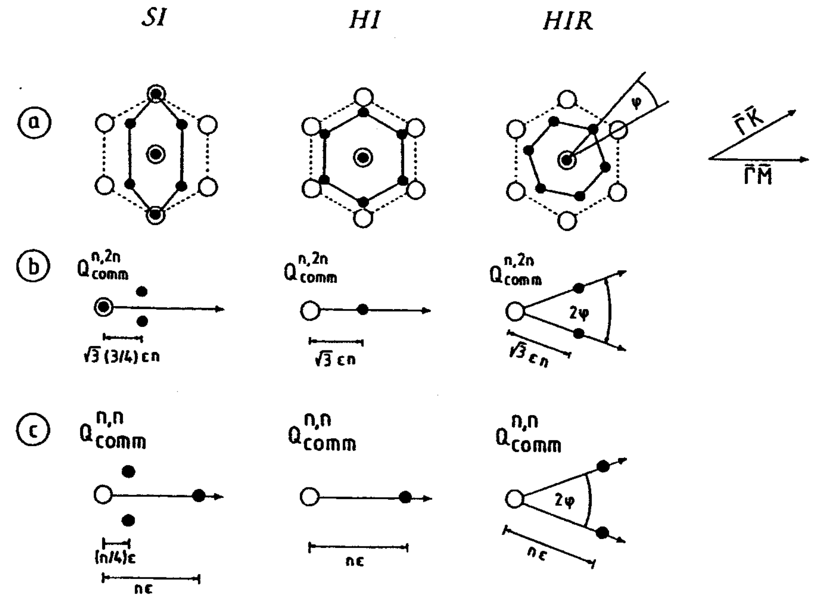

Fig.2.11. a) Real lattice and b,c) schematic representation of the (n,n) and (n,2n) diffraction features of various incommensurate structures. SI: striped incommensurate, HI: hexagonal incommensurate, and HIR: hexagonal incommensurate rotated. All phases are assumed to be fully relaxed. o denotes the $(\sqrt{3}x\sqrt{3})R30^o$ commensurate and • the incommensurate structures

is observed (with $Q^{2,2}_{comm}$ = 3.02 Å^{-1}); whereas the $(1,2)_{Xe}$ pattern consists of a single peak at the commensurate position and a shallow doublet with the maximum intensity at about $Q^{1,2}_{comm}$ + 0.13 Å^{-1} (with $Q^{1,2}_{comm}$ = 2.62 Å^{-1}). The observed incommensurability deduced from the well-defined polar location of the peaks in Fig.2.12a is ϵ = 0.95 Å and corresponds to an interrow distance in the $\overline{\Gamma M}$ direction of d_{SI} = 3.91 Å. This results in a misfit m = 1-d_{SI}/d_C = 0.059, where d_c = 4.80·cos30° Å is the inter-row distance of the commensurate Xe structure in the same direction. From the measured polar and azimuthal peak widths in Fig.2.12 we can also estimate average domain sizes of the incommensurate layer. For the $\overline{\Gamma K}$ direction, i.e, parallel to the walls, we obtain ≃350 Å and for the perpendicular $\overline{\Gamma M}$ direction ≃50 Å.

The analysis in the last paragraph has shown that the incommensurate Xe layer on Pt{111} at misfits of about 6% is a striped phase with the domain walls strongly relaxed, i.e., a uniaxially compressed layer. Indeed, for less relaxed domain walls, depending on the extent of the wall relaxation and on the nature of the walls (heavy or superheavy) additional satellites in the (n,n) diffraction patterns should

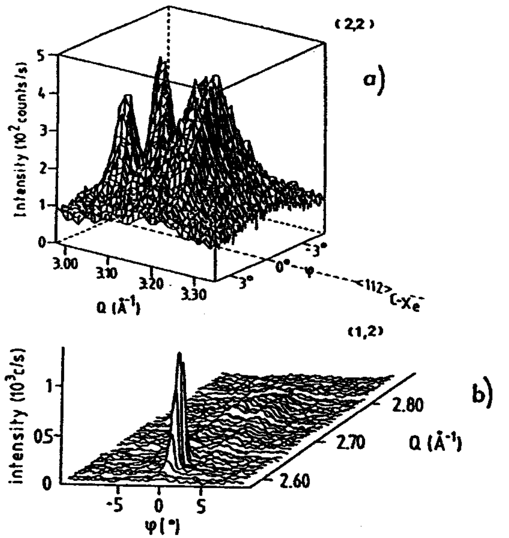

Fig.2.12. 3D-diffraction plot of the a) $(2,2)_{Xe}$ and b) $(1,2)_{Xe}$ diffraction features during the C-I transition at T = 54 K. Q denotes the wave vector in the $\bar{\Gamma}\bar{M}$- and $\bar{\Gamma}\bar{K}$-direction, respectively, while ϕ denotes the azimuthal angle

appear. In the case of a weakly incommensurate layer (misfits below $\simeq$3%) we observe an additional on-axis peak at $Q^{2,2}_{comm} + \epsilon/2$ in the (2,2) diffraction pattern. In order to determine the nature of the domain walls, we have calculated the structure factor for the different domain wall types as a function of the domain wall relaxation [2.46] following the analysis of *Stephens* et al. [2.47]. The observed additional on-axis satellite at $Q^{2,2}_{comm} + \epsilon/2$ in the weakly incommensurate phase is consistent with the occurrence of superheavy striped domain walls, and the observed peak intensities can be reproduced with a domain wall width of $\lambda \simeq$ 3-5 Xe inter-row distances.

In Fig.2.13, we have analyzed the data of the C-SI transition in the weakly incommensurate phase with a least-squares fit of a power law form $m = m_o(1-T/T_c)^\beta$; the best fit parameters are T_c = 61.7 K, m_o = 0.18 and $\beta = 0.51 \pm 0.04$. The value of β is in good agreement with the Pokrovsky-Talapov prediction. Only data points up to misfits of about 4% have been included in the fit. The cutoff at $\simeq$ 4% has been chosen in accordance with *Erbil* et al. [2.48], who have found the $\beta = 1/2$ power law to be only valid in this range for bromine intercalated graphite. For larger values, the misfit variation with reduced temperature is roughly linear; in this region the inter-wall distance is of order of the wall width and the PT-theory not applicable.

In contrast to the C-I transition of Kr on graphite [2.49], which is in fact a melting transition due to the instability of the hexagonal

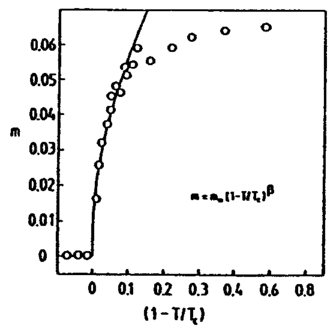

Fig.2.13. $\bar{\Gamma}\bar{M}$-uniaxial misfit m versus reduced temperature during the C-SI transition. The solid line represents the power law fit

weakly incommensurate phase with respect to the formation of free dislocations (reentrant melting), the C-SI transition of Xe/Pt{111} is a solid-solid transition with the incommensurability simply related to the domain wall density. According to *Coppersmith* et al. [2.50], striped structures are stable if the number of sublattices, p (here, 3), is larger than $8^{1/2}$, whereas for hexagonal structures the criterion is p > 7.5±1.5. As mentioned, the critical exponent $\beta = 0.51 \pm 0.04$ deduced from the data in Fig.2.13 is in good agreement with the $\beta = 1/2$ prediction of Pokrovsky and Talapov. The Pokrovsky-Talapov model may essentially be applied to a substrate of uniaxial symmetry, although the original model calculations are performed for an isotropic substrate; thus, it should be applicable to the isotropic Pt{111} substrate. However, in a recent study, *Haldane* and *Villain* [2.51], pointed out that in the case of rare-gas monolayers on metal surfaces, substrate induced electric dipole interactions might be responsible for the square root law. Moreover, they inferred that even in the case of an insulating substrate (no induced dipole forces) the square root behavior should be valid, but only for very small misfits (m<0.001 !). At present, it is difficult to make a choice between the thermal fluctuation mechanism of Pokrovsky and Talapov and the substrate induced dipole mechanism of Haldane and Villain. However, it is worth noting that the experimental range of validity of the square root law in 2D-striped domain wall phases has been found to be much larger (a factor of $\simeq$30) than the limit given by Haldane and Villain, for "insulating" substrates (Br intercalated graphite [2.48]) as well as for metal substrates (Xe/Cu{110} [2.52], Xe/Pt{111} [2.45]).

The width of the superheavy domain walls in the striped phase, as obtained from an analysis of the satellite peak intensities, amounts to 3-5 inter-row distances (FWHM). With increasing incommensurability, the total length of the domain walls is expected to increase, while the wall thickness is expected to remain constant [2.53], giving rise to smaller and more numerous commensurate domains. For misfits larger than 3-4%, i.e., where the inter-wall distance becomes less than three times the wall width, the diffraction pattern of the striped incommensurate layer can no longer be distinguished from an unaxially compressed layer.

The most direct implication of the existence of a striped phase in Xe layers on Pt(111) is that the wall crossing energy is substantially positive. This is at variance with observations made for Kr layers on graphite [2.49], where the crossing energy was always found to be negative or at least only slightly positive (so that the entropy gain due to the free breathing of the honeycomb lattice is sufficient to stabilize the hexagonal symmetry). *Gooding* et al. [2.54] have studied the influence of the substrate potential modulation on the different wall energies. They found that for large potential modulations striped arrays of discommensuration might have lowest energy. This goes along with the large potential modulation observed for the Xe/Pt(111) system [2.55]. The extended misfit range ($0<m<7.2\%$) in which the striped structure appears to be stable, is somewhat puzzling in view of recent theoretical results by *Halpin-Healy* and *Kardar* [2.56]. They have studied the occurrence of striped structures in the "striped helical Potts lattice gas model". Their results reveal a strong correlation between the extent of the striped phase regime and the wall thickness. Striped structures in an extended coverage range should appear only for "sharp" domain walls: with increasing wall thickness this range is expected to shrink substantially. The energy cost due to the wall repulsion seems to be too large for thick walls. They conclude that the wall width of 4-5 inter-rows in Kr monolayers on graphite [2.57] might be responsible for the absence of a striped phase in this system. The wall width in Xe layers on Pt(111) is similar; the coverage range in which the striped phase is found to be stable corresponds in Halpin-Healy and Kardars calculations to wall widths of 1-2 inter-rows.

When increasing the misfit above 6.5%, an additional on-axis peak at $Q^{1,2}_{comm} + \sqrt{3}\epsilon$ appears in the (1,2) diffraction spots (Fig.2.14). This marks the transition from the striped to the hexagonal incommensurate phase. Diffraction patterns composed of a peak at $Q^{1,2}_{comm}$ and a doublet at $Q^{1,2}_{comm} + (3/4)\sqrt{3}\epsilon$ originating from a SI phase, and an on-axis peak

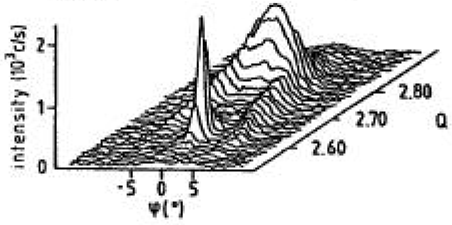

Fig.2.14. 3D-diffraction plot of the $(1,2)_{Xe}$ diffractional feature of an incommensurate Xe layer on Pt(111) at misfit of 7.0% ($\theta_{Xe} = 0.35$, T = 25 K.)

at $Q^{1,2}_{comm} + \sqrt{3}\epsilon$ originating from a HI phase are observed in the misfit range $6.5\% \leq m \leq 7.3\%$, with the HI peak intensity progressively increasing with coverage. We thus conclude that the SI phase transforms at misfits of $\simeq 6.5\%$ to a HI phase in a first order transition. Xe on Pt(111) appears to be the first 2D system fully consistent with the BMVW theory, i.e., the first system displaying the full sequence of C $\rightarrow$ SI $\rightarrow$ HI transitions with increasing incommensurability. Of course, the BMVW theory is a T = 0 K theory neglecting thermal fluctuation effects. However, *Halpin-Healy* and *Kardar* [2.58] have recently studied the various domain wall phases in the framework of a generalized helical Potts model, including finite temperature effects and two species of domain walls. Their results were in general agreement with the BMVW theory; in particular, they pointed out that the C $\rightarrow$ SI $\rightarrow$ HI sequence only occurs when assuming repulsive heavy and super-heavy wall crossings. This is confirmed by the Xe/Pt(111) system.

2.2.4 Can High Order Commensurate Adlayers be Distinguished from Incommensurate Ones?

In the commensurate structure discussed in the last paragraph, all adatoms are located in equivalent high symmetry sites. Here, we will focus on overlayers where only a fraction of the adatoms occupies equivalent sites, layers which have been defined as high order commensurate (HOC). *Aubry* has studied the occurrence of such HOC phases at T = 0 K in a one-dimensional model [2.59]. His study revealed the unexpected result that upon variation of the chemical potential the overlayer will lock successively into all high order commensurate wavevectors and that there are no incommensurate phases in between. Thus, the wavevector varies continuously, but nonanalytically; a form which is known as a devil's staircase. The notion of a devil's staircase is somewhat academic, because finite temperature effects have been neglected in Aubry's theory. Indeed, a layer is only locked, i.e., can be regarded as high order commensurate, if the energy gain due to the occupation of the potential minima by a fraction of the adatoms is large compared to the temperature.

Until very recently there has been no convincing experimental evidence for the existence of high order commensurate physisorbed layers. This appeared to support the widespread belief that "experimentally it is impossible to distinguish between a HOC structure and an incommensurate structure" (*Per Bak* in [Ref.2.60, p.587]). This statement is certainly true if the only accessible experimental information is the ratio of the adlayer and substrate wavevectors from a diffraction experiment. Indeed, because one can always find one rational number within the confidence range of any experimental irrational number, i.e., the wavevector ratio supplied by the most refined experiment is always compatible with a high order commensurate phase. We will show here, however that there are at least four other criteria which allow an unequivocal distinction between high order commensurate and incommensurate. In a recent letter [2.61], we have proposed and demonstrated two criteria based on thermal expansion and adlayer buckling, respectively:

i) *Thermal expansion*

An incommensurate "floating" rare-gas layer is expected to thermally expand very much like the corresponding rare-gas bulk crystal, whereas a commensurate "locked" layer has to follow by definition the substrate at which it is locked. The thermal expansion of rare-gas solids being at least ten times larger than that of substrates normally used, the distinction between HOC and I becomes straightforward. Indeed, the thermal expansion criterion is a very sharp criterion, because it requires that the "locking" is strong enough to withstand temperature variatons over a sufficiently large range ($\geq$10K) to allow for reliable thermal expansion measurements.

ii) *Commensurate buckling*

The locking of a high order commensurate adlayer is due to a fraction of the adlayer being located at high symmetry, high bonding substrate sites. These stronger bound atoms are located "deeper" in the substrate surface than the others; the adlayer is periodically buckled. This buckling superstructure should give rise to additional satellites in a diffraction experiment. Due to the extreme sensitivity of He-scattering to the surface topography these satellites can be detected by high resolution He-diffraction.

There are two additional criteria which, in principle, could be used to distinguish between I and HOC. The present state of the experimental techniques, however, is the main hurdle in applying them. Neither in-plane phonons, nor adsorbed layers of sufficient spatial coherence are yet accessible.

iii) *Lattice dynamical criterion*

A basic property of all commensurate layers (C as well as HOC) is that they have discrete rather than continuous character and that infinitesimal displacements of the whole layer cost a nonzero amount of energy; i.e., the commensurate layers are "locked" on the substrate. According to the general theorems of lattice dynamics, the broken translational invariance requires that the longitudinal and transverse phonon branches of HOC monolayers are optical modes (finite frequency at the $\bar{\Gamma}$ point). On the other hand, in incommensurate layers the monolayer can be shifted with respect to the substrate by an

arbitrary vector without change in energy. Due to this reestablished translational invariance the in-plane vibrational modes become acoustic (zero frequency at the $\bar{\Gamma}$ point).

iv) *Bragg peak singularities*

In 3D crystals with perfect long-range order, the structure factor S(Q) exhibits delta-function singularities, i.e., the Bragg peaks. As already stated, there is no real long-range positional order for incommensurate monolayers with continuous symmetry. Due to the algebraic decay of positional correlation, as proved by Jancovici, there is only a power law singularity of the form

$$S(Q) \simeq \sum_{G} \left| Q^{\parallel} - G_m \right|^{-2+\eta_G} . \qquad (2.13)$$

Since long range positional correlations in a commensurate monolayer are recovered by pinning to the substrate, the structure factor from a commensurate 2D layer exhibits delta function singularities at the diffraction conditions. Thus, a careful peak shape analysis could be used to distinguish between HOC and I.

2.2.5 The I-HOC Phase Transition of Monolayer Kr on Pt{111}

Figure 2.15a shows a series of polar He scans of the $(1,1)_{Kr}$ diffraction peak taken at 25 K along the $\bar{\Gamma}\bar{M}_{Kr}$ direction of Kr monolayers adsorbed on a Pt{111} surface at coverages between 0.5 and 0.95 ML. The sequence is characteristic for a first order phase transition from a hexagonal solid phase with wavevector Q = 1.769 Å^{-1} (d_{Kr} = 4.10 Å) to one with Q = 1.814 Å^{-1} (d_{Kr} = 4.00 Å), below and above 0.8 ML, respectively. During the phase transition, the intensity diffracted from one phase increases at the expense of the other.

The question concerning the incommensurate "floating" versus high order commensurate "locked" nature of the two Kr-phases has been addressed by looking at their thermal expansion behavior and by searching for superstructure satellites. In Fig.2.15b the measured Kr-Kr interatomic spacing versus temperature is shown for submonolayer films of coverage 0.5 ML and 0.95 ML. The difference is striking. The low coverage phase shows a variation with temperature, very much like bulk Kr (dashed), and is thus an incommensurate "floating" phase. In contrast, the lattice parameter of the high coverage phase is - like that of the Pt substrate (solid) - constant within experimental error in the same temperature interval; accordingly, this Kr-phase is high-order commensurate "locked".

This assignment is supported by inspection of Fig.2.16a, where polar scans (He-beam energy 12 meV) in the $\bar{\Gamma}\bar{K}_{Kr}$ direction of the

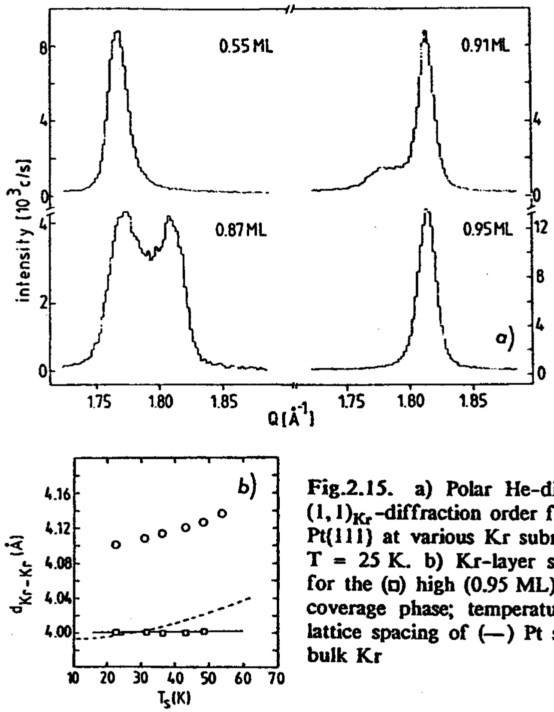

Fig.2.15. a) Polar He-diffraction scans of the $(1,1)_{Kr}$-diffraction order from Kr monolayers on Pt(111) at various Kr submonolayer coverages at T = 25 K. b) Kr-layer spacing vs temperature for the (□) high (0.95 ML) and (o) low (0.5 ML) coverage phase; temperature dependency of the lattice spacing of (—) Pt substrate, and of (---) bulk Kr

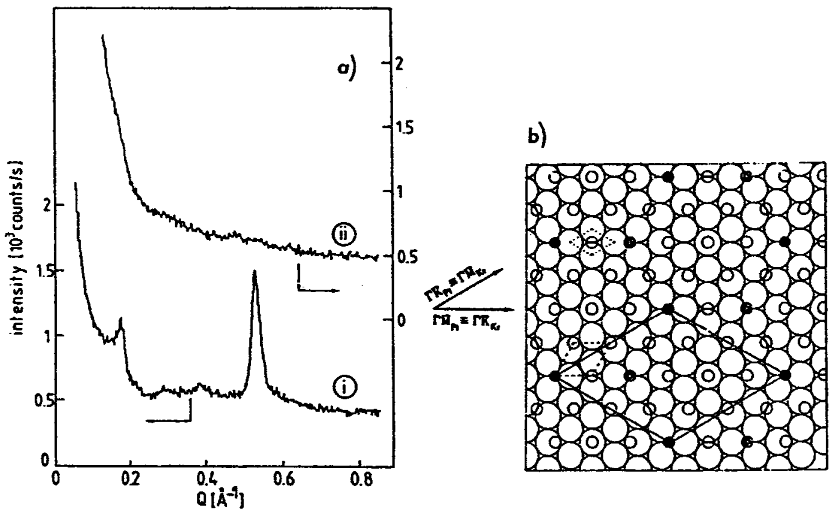

Fig.2.16. a) Polar He-diffraction scans of Kr monolayers in the vicinity of the specular peak (Q = 0 Å^{-1}); i) high (0.95 ML) and ii) low (0.5 ML) coverage phase, taken along the $\bar{\Gamma}\bar{K}_{Kr}$-azimuth. b) Schematic representation of the high coverage phase of Kr on Pt(111); small circles represent Kr-atoms (d_{Kr-Kr}=4.00 Å) and large circles the Pt substrate atoms (d_{Pt-Pt}=2.77 Å)

"floating" and of the "locked" Kr layer are shown. The scans differ substantially: the locked scan clearly evidences the presence of a superstructure, while the floating one does not. The superstructure peak at Q = 0.532 ± 0.022 Å^{-1} corresponds to 1/5 of the Pt substrate principal lattice vector. The origin of the superstructure peak is illustrated on the right hand of Fig.2.16b where the "locked" Kr phase on the Pt(111) surface is schematically shown. The Kr layer is rotated by 30° with respect to the substrate and its translational position is fixed by locating the central Kr atom in a preferred three-fold hollow site (say fcc). Obviously, the Kr atoms in fcc sites (filled small circles) form a hexagonal (5 x 5)R0° superstructure, which is responsible for the diffraction satellite at $Q_{Pt}^{1,1}/5$. Note that the superstructure is aligned with the substrate lattice while the Kr layer as a whole is rotated by 30°; this is the reason why the superstructure satellite is seen in the $\bar{\Gamma}\bar{M}_{Pt} = \bar{\Gamma}\bar{K}_{Kr} = \bar{\Gamma}\bar{M}_{superstructure}$-direction. The particular ratio between the lattice parameters of adlayer and substrate $\sqrt{3}\ d_{Pt}/d_{Kr} = 6/5$ produces an additional peculiarity: the same number of Kr atoms are located in hcp and fcc hollow sites. Thus the (5 x 5)R0° superstructure of the locked Kr atoms has a two-atomic basis. A simple counting in Fig.2.15b shows that one sixth of the Kr atoms are locked in a hollow site (fcc or hcp). This fraction appears to be sufficient to hinder the Kr layer from expanding freely over more than 25 K.

The correlation between negligible thermal expansion and the presence of a periodic adlayer buckling in the high coverage phase of Kr on Pt(111) unequivocally demonstrates the high order commensurate character of this phase. The superstructure peak in Fig.2.16a originates certainly from the layer buckling due to a fraction of Kr atoms located in high symmetry sites of the substrate. Indeed, the Kr layers being oriented along high symmetry axes of the substrate, there is no reason for the occurrence of mass density wave satellites (see below) which might complicate the interpretation [2.62].

2.2.6 Rotational Epitaxy of Monolayers

In the one-dimensional chain model of Frank and van der Merwe, the longitudinal misfit strain of the incommensurate layer is minimized by the formation of misfit dislocations. As demonstrated above, the formation of misfit dislocations - domain walls - also minimizes the total energy of an incommensurate 2D-layer close to the C-I transition (i.e., at small misfits). In two dimensional incommensurate overlayers, however, longitudinal as well as transverse strains are present. Since transverse strains have lower energy than longitudinal strains in a 2D-layer (transverse phonons are softer than longitudinal ones), the interconversion of these strains may minimize the total energy of the overlayer by rotating the adlayer out of the symmetry axes of the substrate.

Indeed, *Novaco* and *McTague* [2.63] have shown that for monolayers far from commensurability these rotations are energetically favorable and the rotation angle ϕ follows a simple relation:

$$\cos\phi = \frac{1 + (1+m)^2(1+2\eta)}{(1+m)[2 + \eta + \eta(1+m)^2]} \qquad \eta > (1+m)^{-1}$$

$$\phi = 0 \qquad \eta < (1+m)^{-1} \tag{2.14}$$

with $\eta = (c_\ell/c_t)^2 - 1$, c_ℓ and c_t being the longitudinal and transverse velocities of sound in the monolayer and m the misfit. For a Cauchy solid we have $c_\ell/c_t = 3^{1/2}$. Novaco and McTague also showed that this rotational epitaxy involves the creation of mass density waves, MDW, (also known as static distortion waves, SDW), i.e., there exists a periodic variation in the position of monolayer atoms from their regular lattice sites. These MDW bear relevant similarities to the charge density waves (CDW) of layered crystals [2.64]. Indeed, it is the combination of rotation and small displacive distortions of the adatom net which allows the adlayer to minimize its total energy in the potential relief of the substrate. In a diffraction experiment, these mass density waves should give rise to additional satellites.

Fuselier et al. [2.65] have introduced an alternative concept to explain the adlayer rotation: the "coincident site lattice". They pointed out that energetically more favorable orientations are obtained for rotated high-order commensurate structures. The larger the fraction of adatoms located in high symmetry sites, the larger the energy gain and the better the rotated layer is locked. It turned out that the predictions of the coincident site lattice concept for the rotation angle versus misfit agrees well with the Novaco-McTague predictions.

The Novaco-McTague rotational epitaxy has been observed in numerous adsorbate systems including Ar [2.66], Ne [2.67], and Kr [2.57] on graphite, Na/Ru{100} [2.68], K/Cu{100} [2.69] and K/Pt{111} [2.70]. It has also been observed for Xe monolayers on Pt {111} at large incommensurabilities [2.71]. As already shown in the last paragraph, the striped incommensurate phase of Xe on Pt{111} transforms above 6.5% misfit to a hexagonal incommensurate phase. When increasing the misfit above 7.2% the striped phase disappears and only the diffraction peaks characterizing the hexagonal phase are observed. However, these diffraction peaks at $Q^{1,2}_{comm} + \sqrt{3}\epsilon$ and $Q^{2,2}_{comm} + 2\epsilon$ (in the (1,2) and (2,2) diffraction patterns, respectively) start to split azimuthally with increasing misfit (Fig.2.17a). This obviously characterizes a Novaco-McTague rotated phase.

Figure 2.17b is a plot of the rotation angle ϕ as a function of the average misfit during the HI-HIR transition; the black dots are the measured data. The dashed line is the Novaco-McTague linear response

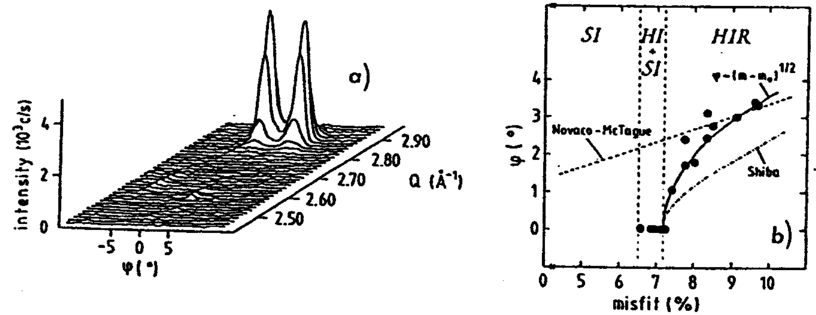

Fig.2.17. a) 3D-diffraction plot of the $(1,2)_{Xe}$ diffraction feature of an incommensurate Xe layer on Pt(111) at a misfit of 9.6% (θ_{Xe}=0.41, T=25 K). b) Rotation angle ϕ of Xe monolayers on Pt(111) versus misfit m

theory for a Cauchy solid (2.14). *Shiba* [2.72] noted that with increasing misfit a crossover from the domain wall regime (small incommensurabilities) to the modulation regime (large incommensurabilities) should occur, and that there should be a finite misfit for the onset of rotation. His curve for a Cauchy solid is also drawn in Fig.2.17b (dashed-dotted) for the value of his parameter ℓ which causes the HI-HIR transition to occur at a critical misfit of 7.2% (here $\ell \simeq 10$). The parameter ℓ in Shiba's theory is analogous to Frank and van der Merwe's ℓ, i.e., is the distance between the domain walls in units of Xe inter-row distances in the $\bar{\Gamma}\bar{M}$ direction at the transition. Shiba's theory gives a qualitative account of the overall variation of rotation angle versus misfit but no quantitative account. Actually, the data are fitted well by a power law of the form $\phi \simeq (m-m_0)^{1/2}$ with m_0 = 0.072, which is shown as a solid line in Fig.2.17b. A similar power law behavior has been observed for the rotation angle of Kr layers on graphite [2.57] and in Cs intercalated graphite [2.73].

The observation of a finite critical misfit for the onset of rotation is also consistent with the approximate analysis of *Villain* [2.74] and the analytic treatment of *Gordon* and *Villain* [2.75]. Both have calculated the energy associated with a small rotation of a system of parallel walls near the C-I transition, and found that the domain wall rotation should take place in the incommensurate regime (i.e., a finite misfit) and not at the C-I transition. The Novaco-McTague model calculations [2.63] have been performed in the linear response approximation of the adsorbate-substrate interaction. Close to the C-I transition, however, this approximation fails and no rotation has to be expected for realistic values of the Lamé coefficients of the adlayer.

It is worthwhile to address here the question concerning the physics behind the rotational epitaxy; mass density waves [2.63] or high-order commensurability [2.65]? In a He-diffraction study from rotated Xe monolayers on Pt{111} we have, indeed, observed satellite peaks and assigned them to a high order commensurate superstructure [2.32]. However, *Mirta Gordon* [2.62] pointed out that these satellites could be due to the MDW. Here, we will show that, indeed, both MDW as well as commensurate buckling satellites are present in the rotated Xe monolayers on Pt{111}. The distinction between the two types of satellites is straightforward. As pointed out by Gordon, the MDW satellites should be subject to the following relation:

$$Q \simeq (8\pi/d^{R}_{Xe})\,(m/\sqrt{3})\,(1 + m/8) \qquad (2.15)$$

where Q is the wavevector of the satellites, m the misfit and d^{R}_{Xe} the lattice constant of the rotated Xe layer. For not too large misfits, the MDW satellites should appear in the same direction as the principal reciprocal lattice vector of the Xe layer, i.e. in the $\bar{\Gamma}\bar{M}_{Xe}$ direction. On the other hand, the commensurate buckling, according to its peculiar structure [Ref.32,Fig.2.3] should have its maximum amplitude in the $\bar{\Gamma}\bar{K}_{Xe}$ direction. Moreover, these commensurate buckling satellites should only be present at the particular coverage where the high order commensurability becomes favorable, in the present case at monolayer completion (m=9.6%) [2.32], whereas the MDW satellites should be present in the entire misfit range where the Xe layer is rotated (7.2%-9.6%).

In Fig.2.18a we show polar He diffraction scans in the vicinity of the specular beam, with the scattering plane oriented along the $\bar{\Gamma}\bar{M}_{Xe}$ direction, for rotated Xe layers of misfit 8.3% and 9.5%, respectively. In both scans satellite peaks are present. The dispersion of these peaks is shown in Fig.2.18b, and compared with Gordon's prediction for the MDW given above. The data follow qualitatively the predicted dependency; the agreement becomes quantitative at misfits larger than ≃ 8%. The reason for the better agreement at large misfits is due to the fact that Gordon's analysis of the MDW (similar to Novaco-MacTague's model calculations) have been performed in the linear response approximation of the adsorbate-substrate interaction. As discussed in connection with Fig.2.17b above, this approximation is only justified at larger misfits. The measured intensities of the MDW satellites vary between 10^{-2} of the strongest Xe layer diffraction peak at small misfits to about 10^{-1} at large misfits. These intensities can be correlated with the amplitudes of the MDW. By means of [2.62,Eq.6-8] and by using realistic values for the Xe/Pt{111} potential (as listed in [2.76]) MDW amplitudes of the order 0.1 Å are obtained.

In Fig.2.19a we show scans like in Fig.2.18a but now measured in the $\bar{\Gamma}\bar{K}_{Xe}$ direction for rotated Xe layers of misfits 8% and 9.6%. At variance with the scans in the $\bar{\Gamma}\bar{M}_{Xe}$ direction (Fig.2.18a), a satellite

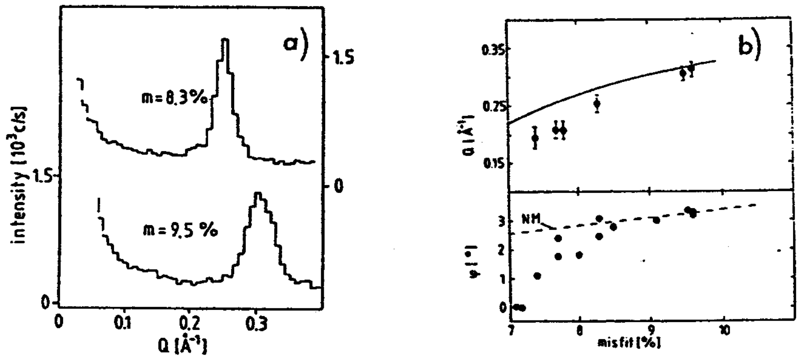

Fig.2.18. a) Polar He-diffraction scans of rotated Xe monolayers on Pt{111} in the vincinity of the specular peak (Q=0 Å^{-1}) taken along the $\bar{\Gamma}\bar{M}_{Xe}$azimuth, at m = 8.3% and 9.5%, respectively. b) Dispersion of the mass density wave (MDW) satellites with misfit m. The solid line is Gordon's relation (2.15)

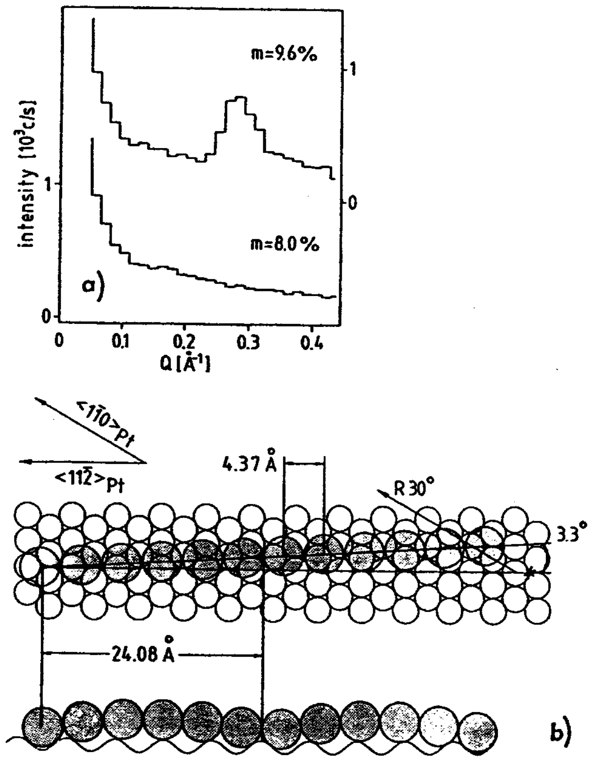

Fig.2.19. a) Polar He-diffraction scans of rotated Xe-monolayers on Pt{111} in the vicinity of the specular peak (Q=0 Å^{-1}) taken along the $\bar{\Gamma}\bar{K}_{Xe}$-azimuth, at m = 8% and 9.6%, respectively. b) Upper and side view of a 3.3° rotated domain of the complete monolayer. The Xe domain is represented schematically by a chain of twelve atoms

peak is observed only for the complete Xe monolayer (m=9.6%). The location of this satellite peak at 0.28 $Å^{-1}$ corresponds to a buckling period of 23 Å and can be ascribed to a high order commensurate structure shown in Fig.2.19b, as described in detail in [2.32]. Being present only at a particular misfit, this peak does not originate from a MDW. Thus, only at monolayer completion (m=9.6%) does the rotated Xe layer lock in the substrate, i.e., becomes a high order commensurate phase.

Thus the present answer to the question addressed is that both mass density waves and high order commensurability may be involved in rotational epitaxy.

2.3 Multilayer Growth of Rare Gases

2.3.1 Dynamical Coupling Between Adlayer and Substrate

The first systematic theoretical and experimental exploration of the dynamics of rare gas monolayers on metal surfaces was performed on Ag{111} [2.77]. The lattice dynamical calculations were based on a simple model - Barker pair potentials - to model the lateral adatom interactions and a rigid holding substrate. The calculations have supplied dispersion curves fully adequate to account for the available experimental data.

As expected from any model involving only central forces between the adatoms and a rigid substrate, the three modes of the monolayer decouple, and the perpendicular mode is dispersionless, i.e., the motion of the adatoms perpendicular to the surface acts like an Einstein oscillator. Because the perpendicular surface atom motions dominate the inelastic He cross sections, this dispersionless mode has, indeed, been observed in the experiments [2.77].

It is noteworthy that the most general conclusion emerging from this first systematic exploration, has been that "coupling between adatom and substrate atom motions is potentially more important than modest variations in the nature of the adatom-adatom potential" [2.77]. *Hall* et al. [2.78] extended their exploration by allowing the substrate atoms to move and by focussing on the coupling between the substrate and adlayer modes. As expected, the results of the calculations show that near the zone boundary $\bar{M}$ (the $\bar{\Gamma}\bar{M}$ direction has been explored), where the substrate phonon frequencies are well above those of the adlayer, the influence of the substrate adlayer coupling is small. Near the zone center $\bar{\Gamma}$ the anomalies introduced by the coupling are twofold:

1. A dramatic hybridization splitting around the crossing between the dispersionless adlayer mode and the substrate Rayleigh wave (and a less dramatic one around the crossing with the $\omega = c_\ell Q^{\parallel}$ line - due to the Van Hove singularity in the projected bulk phonon density of states);

2. A substantial line width broadening of the adlayer modes in the whole region near $\bar{\Gamma}$ where they overlap the bulk phonon bands of the substrate: the excited adlayer modes may decay by emitting phonons into the substrate; they become leaky modes. These anomalies were expected to extend up to trilayers even if more pronounced for bi- and in particular for monolayers. More recent experimental data of *Gibson* and *Sibener* [2.79] qualitatively confirm these predictions, at least for monolayers. The phonon line widths appear to be broadened around $\bar{\Gamma}$ up to half of the Brillouin zone. The hybridization splitting could not be resolved, but an increase of the inelastic transition probability centered around the crossing with the Rayleigh wave and extending up to 3/4 of the zone has been observed and attributed to a resonance between the adatom and substrate modes.

Recent measurements performed on Ar, Kr and Xe layers on Pt{111} [2.80] with a substantially higher energy resolution ($\Delta E_I \leq 0.4$ meV) have now confirmed the theoretical predictions on the coupling effects within almost every detail (except for the hybridization around the Van Hove singularity, which has not been seen in spite of substantial effort). The sequence of He TOF spectra in Fig.2.20a taken along the $\bar{\Gamma}\bar{M}$ direction of the superstructure of the high-order commensurate (5x5) complete Kr-monolayer identical to the $\bar{\Gamma}\bar{M}_{Pt} = \bar{\Gamma}\bar{K}_{Kr}$ directions (Sect.2.2.5) at 25 K gives a vivid picture of the coupling effects. The last spectrum $\theta_i = 37°$ taken near the zone boundary $\bar{M}$ exhibits a unique, sharp loss $E \simeq -3.7$ meV resulting from the creation of an Einstein Kr-monolayer phonon (perpendicular Kr-Pt vibration); its width corresponds to the instrumental width of $\Delta E_I \simeq 0.38$ meV; as expected there is no linewidth broadening near the zone boundary. On the other hand, the main peak in the first spectrum (θ_i=40°) taken near the $\bar{\Gamma}$-point located at $E \simeq -3.9$ meV and which corresponds also to the creation of a Kr monolayer phonon is broadened by more than 0.5 meV. Of particular interest is the small peak at $E \simeq -3.1$ meV, close to the position of the Pt substrate Rayleigh wave. The next two spectra $\theta_i = 39.5°$ and 39° taken always closer to the crossing between the Pt substrate Rayleigh wave and the Kr Einstein mode demonstrate strikingly the effect of the hybridization of the two modes: the originally tiny Pt-peak increases dramatically, while the Kr-peak is pushed slightly toward larger energies. After passing the crossover, the higher energy loss disappears abruptly. As predicted [2.78] the two features in the doublet only have comparable intensity quite near the crossover.

In Fig.2.20b we show the dispersion curve of the Kr-monolayer obtained from a large number of spectra like those in Fig.2.20a. The

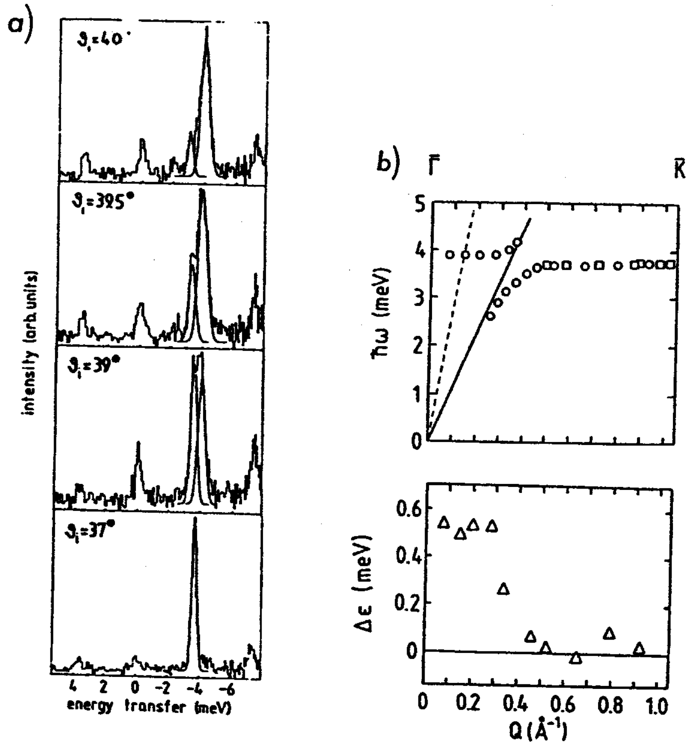

Fig.2.20. a) He energy loss spectra from a Kr monolayer taken along the $\bar{\Gamma}\bar{K}_{Kr}$-azimuth. With decreasing angle phonons with larger wave vector are probed.
b) Experimental dispersion curve of the Kr monolayer and measured linewidth broadening $\Delta\epsilon$ of the Kr creation phonon peaks. The solid line in the dispersion plot is the clean Pt{111} Rayleigh phonon dispersion curve and the dashed line the longitudinal bulk band edge of the Pt{111} substrate both in the $\bar{\Gamma}\bar{M}_{Pt}$ azimuth which is coincident with the $\bar{\Gamma}\bar{K}_{Kr}$ azimuth

hybridization splitting around the crossover with the substrate Rayleigh wave (solid line) is clearly observed. The predicted tiny frequency upshift around the $\bar{\Gamma}$-point due to the coupling to the substrate vibrations is also seen.

The observed line width broadening is also shown in Fig.2.20b. As a measure of the broadening the quantity $\Delta\epsilon = [(\delta E)^2 - \Delta E_I^2]^{1/2}$, with δE the full width at half maximum of the major loss feature and ΔE_I the intrinsic instrumental broadening (ΔE_I=0.38 meV in the present experiment) is plotted as a function of the wave vector. For the ML a broadening larger than 0.5 meV is seen, and - as predicted - confined to the region near $\bar{\Gamma}$, where the adlayer mode overlaps the bulk bands of the substrate.

2.3.2 Layer-by-Layer Evolution of the Lattice Dynamics

In Fig.2.21a we show some characteristic He energy loss spectra which have been measured under identical scattering conditions (θ_i= 42°, E_i=18.4 meV) from Xe-films 1,2,3 and 25 monolayers thick adsorbed on Pt{111}. The kinematical conditions have been chosen to sample energy losses (phonon creation) with small momentum transfer, i.e., to probe the phonon dispersion near the zone center. Due to the high energy resolution, the different losses of the four films are clearly resolved. This makes it possible to straightforwardly determine the completion of each of the first two monolayers within a few percent. This kind of information, which can hardly be obtained with this accuracy by other methods, is very useful, for instance, in deducing thermodynamic properties of multilayer adsorption [2.38].

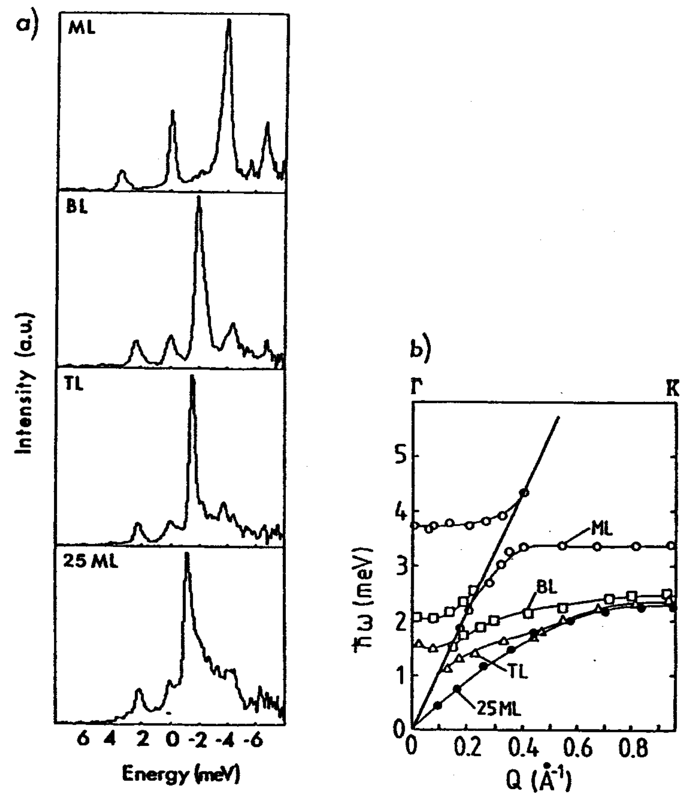

Fig.2.21. a) Energy loss spectra from Xe films on Pt{111}: ML: monolayer, BL: bilayer, TL: trilayer and 25 ML film
b) Experimental dispersion curves of the various Xe films along the $\bar{\Gamma}\bar{K}_{Xe}$ azimuth

By varying the scattering angle, complete phonon dispersion curves for each film have been obtained. This is exemplified in Fig.2.21b, which is a reduced zone plot of the phonon dispersion along the $\bar{\Gamma}\bar{K}$-azimuth of the Xe layers. The layer-by-layer evolution of the surface lattice dynamics with increasing film thickness is obvious. From the initial Einstein-mode for the monolayer a well developed Rayleigh mode (25 ML), characteristic for semi-infinite crystals is approached upon increase of the film thickness. It is noteworthy, that the phonon anomaly, due to the dynamical coupling between substrate Rayleigh wave and adlayer mode, is also present in the bi- and even the trilayer films. It is only the Q-range of the anomaly which becomes smaller, and its location shifts towards the zone center following the location of the intersection between the Xe and the substrate Rayleigh mode. Linewidth broadening, due to radiative damping into the substrate bulk bands has been found to be still substantial for bilayer films, while the trilayer shows no evidence for additional broadening. These results demonstrate that the influence of the substrate on adsorbed multilayer films is extended over several layers rather than being restricted to the first layer only.

2.3.3 Growth Mode and the Scale of Substrate Strength

The mode of nucleation and initial growth of thin films is a matter of longstanding interest. The basic question posed as long as 60 years ago is: given a known substrate/adsorbate, can the growth mode be predicted using atomistic principles only? From thermodynamics we know that when we coat a substrate s with a deposite d under an atmosphere v with which d coexists, three categories of initial film formation can occur [2.81]. These types of film growth can be classified using the surface tension σ. For a droplet of deposit d adsorbed on substrate s in equilibrium we have:

$$\sigma_{sv} = \sigma_{ds} + \sigma_{dv}\cos\theta \qquad (2.16)$$

where σ_{sv}, σ_{ds} and σ_{dv} are the surface tensions of the substrate-vapor, deposit-substrate, and deposit-vapor interfaces and θ is the contact angle (see Fig.2.22a for definition). Equation (2.16) is known as *Young's* equation [2.82].

The deposit wets the substrate completely when $\sigma_{sv} = \sigma_{ds}+\sigma_{dv}$, i.e., $\theta = 0$; the growth occurs layer-by-layer (Fig.2.22b). This growth mode is also known as Frank-van der Merwe or type 1 growth. When $\sigma_{sv} > \sigma_{ds}+\sigma_{dv}$ the deposit grows in a few layers on top of which 3D-islands are formed (Fig.2.22c). This growth mode is also known as partial wetting, Stranski-Krastanov or type 3 growth. When $\sigma_{sv} < \sigma_{ds} + \sigma_{dv}$, i.e., θ is finite, small 3D-cluster are nucleated directly on top of

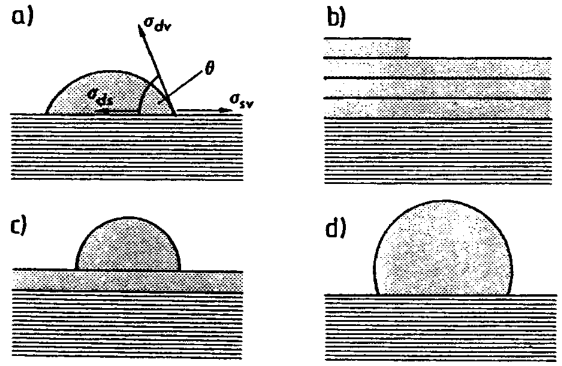

Fig.2.22. Schematic representation of the various growth modes.
a) definitions, b) complete wetting, c) partial wetting, and d) incomplete wetting

the substrate surface which eventually agglomerate into a continuous film (Fig.2.22d). This growth mode is also known as imcomplete wetting, Volmer-Weber or type 2 growth.

It has been suggested by *Sullivan* [2.83], that the determining parameter for the growth mode is the relative substrate strength u/h, which is the ratio of u, the adsorbed-substrate interaction, to h, the lateral adsorbate-adsorbate interaction. *Pandit*, *Schick* and *Wortis* [2.84], based on this idea, have developed a lattice-gas model of adsorption generating detailed phase diagrams of multilayer-adsorption (including wetting behavior, wetting transitions, roughening transitions, melting transitions, etc.) which qualitatively scale with the ratio u/h. Their results are too extensive as to be reviewed here. However, the basic result was that incomplete wetting should take place for low, partial wetting for intermediate, and complete wetting for large relative substrate strengths.

Shortly after, experiments designed to test the theory showed that, in contrast to the predictions, at low temperatures complete wetting is restricted to a very narrow intermediate range of substrate strengths [2.85]. Both, small as well as large u/h values resulted in incomplete wetting behavior

The reentrant wetting behavior (at large u/h) has been explained by the incompatibility between the crystal structure of the monolayer and that of the bulk adsorbate [2.86-88]. Strong substrates tend to compress the adsorbate monolayer beyond the density of close packed planes of the bulk solid to be grown. Since the next adsorbing layers tend to grow epitaxially on the monolayer they are also compressed and the stress in the layer will grow linearly with increasing thickness, preventing complete wetting. For weak substrates the argument is

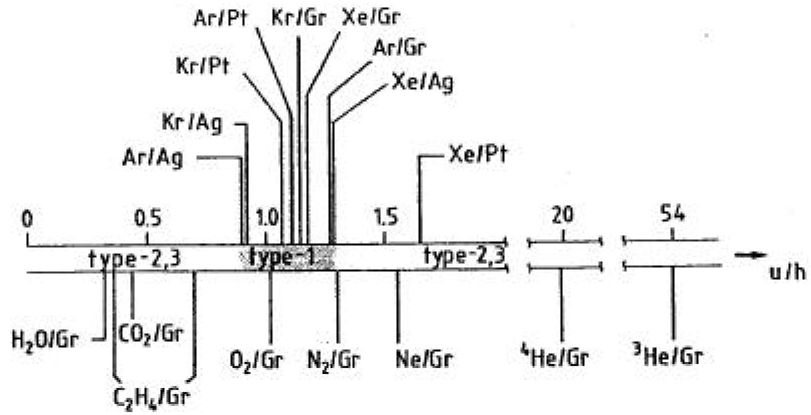

Fig.2.23. Adsorbate-substrate systems ordered on the scale of substrate strengths. Systems exhibiting complete wetting are marked by bars above the center line, while those showing incomplete wetting are indicated below

similar, but now the density in the monolayer is lower than in the bulk solid. Thus, only for intermediate substrate strengths does a compatibility between the structure of the monolayer and that of the bulk adsorbate allow a uniform layer-by-layer growth.

However, this is not the whole truth as can be seen from Fig.2.23, where we show the adsorbate sytems investigated so far ordered on the scale of substrate strengths. The isosteric heat of adsorption is taken for u and the 0 K cohesive energy of the bulk phase of the adsorbing gases for h. Systems exhibiting complete wetting are marked by bars above the center line while those showing incomplete wetting are indicated below. Whereas most systems are in agreement with the reentrant wetting behavior, Xe/Pt{111} exhibits complete wetting although it is located well within the incomplete wetting range. As will be shown in the next section, this anomaly is probably due to registry effects in the Xe/Pt{111} system which result in a neglibible incompatibility between the bulk adsorbate and the full monolayer.

2.3.4 Epitaxial Layer Growth of Xe on Pt{111}

The He energy loss spectra shown in Fig.2.21a not only contain lattice dynamics information as discussed in Sect.2.3.2; they also contain direct information concerning the growth characteristics of the Xe multilayers. This information is in the diffuse elastic peak, i.e., in the peak at zero energy exchange. This peak originates from scattering at impurities and defects and its intensity is a sensitive measure of surface disorder. From the comparison with spectra taken from surfaces of known disorder, we can infer that the monolayer is well ordered and the multilayers even better. For the 25 ML thick film in

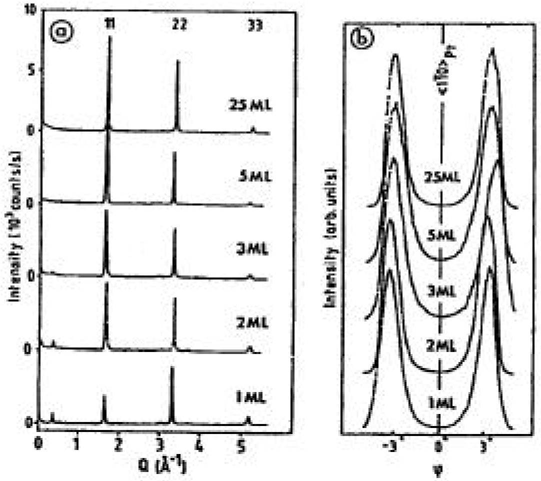

Fig.2.24. a) Polar and b) azimuthal diffraction patterns of Xe films of indicated thickness. The incident plane for the polar patterns was oriented through the left-hand peaks in the azimuthal patterns. All polar patterns are plotted on the same scale; the azimuthal patterns are normalized

Fig.2.21a, the diffuse elastic peak has nearly vanished. This shows that the 25 ML film is very flat, and thus that Xe on Pt{111} exhibits complete wetting. This goes along with the layer-by-layer evolution of the surface phonon dispersion discussed in Sect. 2.3.2.

The structure of the Xe multilayers has been characterized by measuring polar and azimuthal He-diffraction scans, shown in Fig.2.24. As already emphasized in Sect.2.2.6, at monolayer completion the Xe monolayer on Pt{111} is a Novaco-McTague rotated layer with rotation angle $\phi = \pm 3.3°$. The azimuthal plots in Fig.2.24 show that all consecutive layers growing on top of the first layer are likewise rotated by $\phi = \pm 3.3°$. Lattice constant and average domain size, as deduced from the polar diffraction plots, are also unchanged with increasing film thickness, i.e., $d_{Xe} = 4.33 \pm 0.03$ Å and average domain size $\simeq 300$ Å, respectively. Thus, the consecutive layers grow epitaxially on the preceding ones. Within experimental confidence there is no mismatch between the nearest neighbor distances in the monolayer ($d_{Xe}^{R\text{-}ML}$= 4.33 Å, T=25 K) and in the bulk Xe (d_{Xe}^{b}=4.34 Å, T=25 K). This structural compatibility, which leads to an unstrained layer-by-layer growth appears to be a direct result of registry forces. Indeed, Xe/Pt{111} being a "strong substrate" system, the monolayer lattice parameter would be expected, in the absence of registry forces, to be compressed well beyond the bulk value. However, as shown in Sect. 2.2.6, at misfits of 9.6% the rotated monolayer locks into an energetically favorable high order commensurate structure. It is this high order commensurate locking of a fraction of adatoms which, by counterbalancing the tendency of the strong substrate to compress the monolayer lattice beyond the bulk value, allows for an unstrained layer-by-layer growth.

Note that the small peak at low Q-values in Fig.2.24a is a MDW satellite already shown in Fig.2.18a for smaller misfit. The very gradual disappearance of the mass density waves with increasing film thickness, again emphasizes that the influence of the substrate on adsorbed multilayer films extends over several layers.

2.4 Conclusion

Rare-gas monolayers on Pt(111) exhibit a marvellous diversity of 2D phases and phase transitions; most of these have been predicted theoretically, but never been seen completely on other substrates so far. Phases and transitions orginate as a function of temperature and coverage from the interplay between interadatom forces and the corrugation of the holding potential. The exploration of these phenomena is essential for the understanding of the fundamentals of 2D-layer structure and dynamics as well as for the epitaxial growth of thicker layers; the initial, decisive step of this growth appears to be determined by the adatom-substrate interaction.

The experimental exploration of the details of the structure and dynamics of all these phases is made possible by the use of high-resolution thermal He scattering. Energy and momentum resolution; sensitivity for disorder, impurities and defects; and non-destructivity are the distinctive features of thermal He scattering, making it an ideal tool for this kind of investigations.

Acknowledgements. The essential contribution of Rudolf David, Peter Zeppenfeld and Bob Palmer to the results presented here is gratefully acknowledged, as are enlightening discussions with John Black, Sam Fain, Harald Ibach, Doug Mills and Steven Sibener. The careful typing of Maria Kober is also gratefully acknowledged.

References

2.1 R.E. Peierls: Helv. Phys. Acta 7, 81 (1934) Suppl.II
2.2 L.D. Landau: Phys. Z. Sowjetunion II, 26 (1937)
2.3 F. Wagner: Z. Phys. 206, 465 (1967)
2.4 B. Jancovici: Phys. Rev. Lett. 19, 20 (1967)
2.5 J.M. Kosterlitz, D.J. Thouless: J. Phys. C 6, 1181 (1973)
2.6 F.F. Abraham: Physics Reports 80, 339 (1981)
2.7 B.I. Halperin, D.R. Nelson: Phys. Rev. B 19, 2457 (1979)
2.8 A.P. Young: Phys. Rev. B 19, 1855 (1979)
2.9 J. Villain, M.B. Gordon: Surf. Sci. 125, 1 (1983), and references therein

2.10 G. Ertl, J. Küppers: *Low Energy Electrons and Surface Chemistry* (Verlag Chemie, Weinheim 1985)
2.11 H. Ibach: J. Vac. Sci. Technol. A 5, 419 (1987)
2.12 M.D. Chinn, S.C. Fain: J. Vac. Sci. Technol. 14, 314 (1977)
2.13 J.A. Venables, J.L. Senguin, J. Suzanne, M. Bienfait: Surf. Sci. 145, 345 (1984)
2.14 J.A. Martin, M.G. Lagally: In *Scanning Electron Microscopy*, ed. by O. Johari (Scanning Electron Microscopy, Inc., Chicago 1985) Vol.4
2.15 K.D. Gronwald, M. Henzler: Surf. Sci. 117, 180 (1982)
2.16 W. Telieps, E. Bauer: Ultramicroscopy 17, 57 (1985)
2.17 J.L. Seguin, J.Suzanne, M. Bienfait, J.G. Dash, J. Venables: Phys. Rev. Lett. 51, 122 (1983)
2.18 D.E. Savage, M.G. Lagally: Phys. Rev. Lett. 55, 959 (1985)
2.19 R.K. Thomas: Prog. Solid. St. Chem. 14, 1 (1982)
2.20 M. Bienfait: Europhys. Lett. 4, 79 (1987)
2.21 P. Eisenberger, W.C. Marra: Phys. Rev. Lett. 46, 1081 (1981)
2.22 D.E. Moncton, G.S. Brown: Nucl. Instr. Meth. 208, 579 (1983)
2.23 E.D. Specht, R.J. Birgeneau, K.L. D'Amico, D.E. Moncton, S.E. Nagler, P.M. Horn: J. de Phys. Lett. 46, L561 (1985)
2.24 E. Burkel, J. Peisl, B. Dorner: Europhys. Lett. 3, 957 (1987)
2.25 G. Brusdeylins, H.D. Meyer, J.P. Toennies, K. Winkelmann: *Rarefied Gas Dynamics*, ed. by J.L. Potter (AIAA, New York 1977) Vol.II
2.26 R. Campargue: J. Phys. Chem. 88, 4466 (1984)
2.27 O. Stern: Naturwiss. 17, 391 (1929)
2.28 J.P. Toennies, K. Winkelmann: J. Chem. Phys. 66, 3965 (1977)
2.29 K. Kern, R. David, G. Comsa: Rev. Sci. Instr. 56, 369 (1985)
2.30 T. Engel, K.H. Rieder: *Structural Studies of Surfaces with Atomic and Molecular Beam Diffraction*, Springer Tracts Mod. Phys., Vol.91 (Springer, Berlin, Heidelberg 1982)
2.31 J.P. Toennies: J. Vac. Sci. Technol. A 2, 1055 (1984)
2.32 K. Kern, R. David, R.L. Palmer, G. Comsa: Phys. Rev. Lett. 56, 2823 (1986)
2.33 A.M. Lahee, J.R. Manson, J.P. Toennies, Ch. Wöll: Phys. Rev. Lett. 57, 471 (1986)
2.34 J.W. Frenken: private communication
2.35 G. Comsa, B. Poelsema: Appl. Phys. A 38, 153 (1985)
2.36 R. David, K. Kern, P. Zeppenfeld, G. Comsa: Rev. Sci. Instr. 57, 2771 (1986)
2.37 G. Comsa, R. David, B.J. Schumacher: Rev. Sci. Instr. 52, 789 (1981)
2.38 K. Kern, R. David, R.L. Palmer, G. Comsa: Surf. Sci. 175, L669 (1986)
2.39 R.L. Park, H.H. Madden: Surf. Sci. 11, 188 (1968)
2.40 F.C. Frank, J.H. Van der Merwe: Proc. Roy. Soc. London Ser. A 198, 216 (1949)
2.41 P. Bak, D. Mukamel, J. Villain, K. Wentowska: Phys. Rev. B 19, 1610 (1979)
2.42 V.L. Pokrovsky, A.L. Talapov: Sov. Phys. JETP 51, 134 (1980)
2.43 K. Kern, R. David, R.L. Palmer, G. Comsa: Phys. Rev. Lett. 56, 620 (1986)
2.44 M.B. Gordon, J. Villain: J. Phys. C 18, 3919 (1985)
2.45 K. Kern, R. David, P. Zeppenfeld, R.L. Palmer, G. Comsa: Solid State Commun. 62, 361 (1987)
2.46 P. Zeppenfeld, K. Kern, R. David, G. Comsa: Phys. Rev. B (1988) to be published
2.47 P.W. Stephens, P.A. Heiney, R.J. Birgeneau, P.M. Horn, D.E. Moncton, G.S. Brown: Phys. Rev. B 29, 3512 (1984)
2.48 A. Erbil, A.R. Kortan, R.J. Birgeneau, M.S. Dresselhaus: Phys. Rev. B 28, 6329 (1983)
2.49 S.C. Fain, M.D. Chinn, R.D. Diehl: Phys. Rev. B 21, 4170 (1980); D.E. Moncton, P.W. Stephens, R.J. Birgeneau, P.M. Horn, G.S. Brown: Phys. Rev. Lett. 46, 1533 (1981)

2.50 S.N. Coppersmith, D.S. Fisher, B.I. Halperin, P.A. Lee, W.F. Brinkman: Phys. Rev. B 25, 349 (1982)
2.51 F.D.M. Haldane, J. Villain: J. de Phys. 42, 1673 (1981)
2.52 M. Jaubert, M. Glachant, M. Bienfait, G. Boato: Phys. Rev. Lett. 46, 1679 (1981)
2.53 F.F. Abraham, W.E. Rudge, D.J. Auerbach, S.W. Koch: Phys. Rev. Lett. 52, 445 (1984)
2.54 R.J. Gooding, B. Joos, B. Bergersen: Phys. Rev. B 27, 7669 (1983)
2.55 K. Kern, R. David, P. Zeppenfeld, G. Comsa: Surf. Sci. 195, 353 (1988)
2.56 T. Halpin-Healy, M. Kardar: Phys. Rev. B 34, 318 (1986)
2.57 K.L. D'Amico, D.E. Moncton, E.D. Specht, R.J. Birgeneau, S.E. Nagler, P.M. Horn: Phys. Rev. Lett. 53, 2250 (1984)
2.58 T. Halpin-Healy, M. Kardar: Phys. Rev. B 31, 1664 (1985)
2.59 S. Aubry: In *Springer Ser. Solid-State Sci.*, Vol.8, ed. by A.R. Bishop, T. Schneider (Springer, Berlin, Heidelberg 1978) p.264
2.60 P. Bak: Rep. Prog. Phys. 45, 587 (1982)
2.61 K. Kern, P. Zeppenfeld, R. David, G. Comsa: Phys. Rev. Lett. 59, 79 (1987)
2.62 M.B. Gordon: Phys. Rev. Lett. 57, 2094 (1986)
2.63 A.D. Novaco, J.P. McTague: Phys. Rev. B 19, 5299 (1979)
2.64 J.A. Wilson, A.D. Yoffe: Adv. Phys. 18, 193 (1969)
2.65 C.R. Fuselier, J.C. Raich, N.S. Gillis: Surf. Sci. 92, 667 (1980)
2.66 C.G. Shaw, S.C. Fain, M.D. Chinn: Phys. Rev. Lett. 41, 955 (1978)
2.67 S. Callisti, J. Suzanne: Surf. Sci. 105, L255 (1981)
2.68 D.L. Doering, S. Semancik: Phys. Rev. Lett. 53, 66 (1984)
2.69 T. Aruga, H. Tochihara, Y. Murata: Phys. Rev. Lett. 52, 1794 (1984)
2.70 G. Pirug, H.P. Bonzel: Surf. Sci. 194, 159 (1988)
2.71 K. Kern: Phys. Rev. B 35, 8265 (1987)
2.72 H. Shiba: J. Phys. Soc. Jpn. 48, 211 (1980)
2.73 T. Clarke, N. Caswell, P.M. Horn: Phys. Rev. Lett. 43, 2018 (1979)
2.74 J. Villain: Phys. Rev. Lett. 42, 36 (1978)
2.75 M.B. Gordon, J. Villain: J. Phys. C 15, 1817 (1982)
2.76 K. Kern, P. Zeppenfeld, R. David, G. Comsa: In *The Structure of Surfaces II*, ed. by J.F. Van den Veen, M.A. Van Hove, Springer Ser. Surf. Sci., Vo.11 (Springer, Berlin, Heidelberg 1988) p.488
2.77 K.D. Gibson, S.J. Sibener, B.M. Hall, D.L. Mills, J.E. Black: J. Chem. Phys. 83, 4256 (1985)
2.78 B.M. Hall, D.L. Mills, J.E. Black: Phys. Rev. B 32, 4932 (1985)
2.79 K.D. Gibson, S.J. Sibener: Faraday Discuss. Chem. Soc. 80, 14 (1985)
2.80 K. Kern, P. Zeppenfeld, R. David, G. Comsa: Phys. Rev. B 35, 886 (1987)
2.81 J.A. Venables, G.D.T. Spiller, M. Hanbücken: Rep. Prog. Phys. 47, 399 (1984)
2.82 T. Young: Philos. Trans. 95, 65 (1805)
2.83 D.E. Sullivan: Phys. Rev. B 20, 3991 (1979)
2.84 R. Pandit, M. Schick, M. Wortis: Phys. Rev. B 26, 5112 (1982)
2.85 M. Bienfait, J.L. Senguin, J. Suzanne, E. Lerner, J. Krim, J.G. Dash: Phys. Rev. B 29, 983 (1984)
2.86 R.J. Murihead, J.G. Dash, J. Krim: Phys. Rev. B 29, 5074 (1984)
2.87 D.A. Huse: Phys. Rev. B 29, 6985 (1984)
2.88 F.T. Gittes, M. Schick: Phys. Rev. B 30, 209 (1984)